# The Resolved Structure of a Low-metallicity Photodissociation Region

N.B. When citing this work, cite the original published paper.

(article starts on next page)

# The Resolved Structure of a Low-metallicity Photodissociation Region

Ilyse Y. Clark[1] , Karin Sandstrom[1] , Mark Wolfire[2] , Alberto D. Bolatto[2] , Jérémy Chastenet[3] , Daniel A. Dale[4] ,
Brandt A. L. Gaches[5,6] , Simon C. O. Glover[7] , Javier R. Goicoechea[8] , Karl D. Gordon[3,9] , Brent Groves[10] ,
Lindsey Hands[1] , Ralf Klessen[7,11,12,13,17] , Ilse De Looze[3] , J. D. T. Smith[14] , Dries Van De Putte[15] , and
Stefanie K. Walch[16]

[1] Department of Astronomy & Astrophysics, University of California, San Diego, 9500 Gilman Drive, La Jolla, CA 92093, USA; iyclark@ucsd.edu
[2] Department of Astronomy, University of Maryland, College Park, MD 20742, USA
[3] Sterrenkundig Observatorium, Universiteit Gent, Krijgslaan 281-S9, 9000 Gent, Belgium
[4] Department of Physics and Astronomy, University of Wyoming, Laramie, WY 82071, USA
[5] Department of Space, Earth and Environment, Chalmers University of Technology, Gothenburg SE-412 96, Sweden
[6] Faculty of Physics, University of Duisburg-Essen, Lotharstraße 1, 47057 Duisburg, Germany
[7] Universität Heidelberg, Zentrum für Astronomie, Institut für Theoretische Astrophysik, Albert-Ueberle-Str. 2, 69120 Heidelberg, Germany
[8] Instituto de Física Fundamental (CSIC), Calle Serrano 121-123, 28006, Madrid, Spain
[9] Space Telescope Science Institute, 3700 San Martin Drive, Baltimore, MD 21218, USA
[10] International Centre for Radio Astronomy Research, University of Western Australia, 7 Fairway, Crawley, WA 6009, Australia
[11] Universität Heidelberg, Interdisziplinäres Zentrum für Wissenschaftliches Rechnen, Im Neuenheimer Feld 225, 69120 Heidelberg, Germany
[12] Harvard-Smithsonian Center for Astrophysics, 60 Garden Street, Cambridge, MA 02138, USA
[13] Radcliffe Institute for Advanced Studies, Harvard University, 10 Garden Street, Cambridge, MA 02138, USA
[14] Ritter Astrophysical Observatory, University of Toledo, Toledo, OH 43606, USA
[15] Department of Physics & Astronomy, The University of Western Ontario, London, ON N6A 3K7, Canada
[16] I. Physics Institute, University of Cologne, Zülpicher Str. 77, 50937, Cologne, Germany

## Abstract

Photodissociation regions (PDRs) are key to understanding the feedback processes that shape interstellar matter in galaxies. One important type of PDR is the interface between H II regions and molecular clouds, where far-ultraviolet radiation from massive stars heats gas and dissociates molecules. Photochemical models predict that as metallicity decreases, the C/CO transition occurs at greater depths in the PDR compared to the H/$H_2$ transition, increasing the extent of CO-dark $H_2$ gas in low-metallicity environments. This prediction has been difficult to test outside the Milky Way due to the lack of high-spatial-resolution observations tracing $H_2$ and CO. This study examines a low-metallicity PDR in the N13 region of the Small Magellanic Cloud (SMC), where we spatially resolve the ionization front, the $H_2$ dissociation front, and the C/CO transition using $^{12}CO$ $J = 2-1$, $3-2$, and [C I] 1–0 observations from the Atacama Large Millimeter/submillimeter Array and near-infrared spectroscopy of the $H_2$ 2.12 1–0 S(1) vibrational line, and H recombination lines from the James Webb Space Telescope. Our analysis shows that the separation between the H/$H_2$ and C/CO boundaries is approximately $0.043 \pm 0.013$ (stat.) $\pm 0.0036$(syst.) pc (equivalent to $0\rlap{.}''146 \pm 0\rlap{.}''042$(stat.) $\pm 0\rlap{.}''012$(syst.) at the SMC's distance of 62 kpc), defining the spatial extent of the CO-dark $H_2$ region. Compared to our plane-parallel PDR models, we find that a constant-pressure model matches the observed structure better than a constant-density one. Overall, we find that the PDR model does well at predicting the extent of the CO-dark $H_2$ layer in N13. This study represents the first resolved benchmark for low-metallicity PDRs.

*Materials only available in the online version of record:* machine-readable table

## 1. Introduction

Photodissociation regions (PDRs) occur where far-ultraviolet (FUV; 6 eV $< h\nu <$ 13.6 eV) photons drive the chemistry and thermal balance of the interstellar medium (ISM). A common type of PDR is created when massive O and B stars ionize their surroundings inside or near a molecular cloud, leading to distinct layers of ionized, atomic, and molecular gas. The PDR extends from the cloud surface, where the radiation emerging from the H II region photoionizes atoms with ionization potential less than

13.6 eV, to deeper layers in the molecular gas where photo-processes can still be important. A classic example of such a region is the Orion Bar PDR (A. G. G. M. Tielens & D. Hollenbach 1985; PDRs4AllTeam et al. 2022). Since PDRs occur wherever FUV photons govern the properties of the ISM, they represent a significant portion of the atomic and molecular gas in a galaxy (A. G. G. M. Tielens & D. Hollenbach 1985; D. J. Hollenbach & A. G. G. M. Tielens 1997, 1999; M. G. Wolfire et al. 2022). Understanding their characteristics and evolution is crucial, as a large part of the molecular gas reservoir potentially fueling future star formation resides in PDRs.

Early PDR studies, including seminal work by A. G. G. M. Tielens & D. Hollenbach (1985), focused on the Orion Bar and emphasized the penetration depth of the FUV radiation into the cloud, set by the ratio of extinction to column density ($A_V/N_H$), and its crucial role in determining the chemical and thermal

---

structure. Recent observations with the Atacama Large Millimeter/submillimeter Array (ALMA; J. R. Goicoechea et al. 2016, 2017, 2025) and James Webb Space Telescope (JWST; R. Chown et al. 2024; A. Fuente et al. 2024; E. Habart et al. 2024; E. Peeters et al. 2024; D. Van De Putte et al. 2024) have pushed the spatial resolution of Orion Bar measurements to 0.0002 pc. This comprehensive multiwavelength, high-resolution data set of the Orion Bar revealed unexpected small-scale filaments and globules ($\sim 10^{-3}$ pc) along with ridges that follow the boundaries of the PDR. In general, the large-scale PDR structure follows plane-parallel geometry, but with many complex embedded small-scale features which are not well understood (P. F. Goldsmith et al. 2008; C. Joblin et al. 2018).

A PDR's structure is expected to be highly dependent on metallicity (M. Röllig et al. 2006) due to effects from changes in heating and cooling rates and decreased dust extinction (e.g., lower $A_V/N_H$). In higher-metallicity regions, abundant species, such as $C^+$ and O, play crucial roles in cooling and regulating the thermal balance. However, with fewer metals, the gas cooling efficiency decreases (A. G. G. M. Tielens 2010; B. T. Draine 2011) due to reductions of important coolants such as [C II]. This effect may be offset by a lower grain photoelectric heating (e.g., K. E. Jameson et al. 2018), caused by a lower abundance of polycyclic aromatic hydrocarbons (PAHs; J. Chastenet et al. 2019), which dominate the photoelectric heating (E. L. O. Bakes & A. G. G. M. Tielens 1994; M. G. Wolfire et al. 1995). The resulting thermal balance determines the distribution of gas temperature in the PDR, which may affect the chemistry and abundance of atoms and molecules.

PDRs are also critical for understanding the cold molecular gas content of the ISM, because they encompass the transition from H to $H_2$ and ionized carbon ($C^+$) to neutral carbon (C) to carbon monoxide (CO). Cold $H_2$ ($T_{gas} \lesssim 100$ K) is hard to directly observe due to the required excitation energy of its rotational levels, $E(H_2) >> kT_{gas}$. Because of this observational limitation, CO is often used to trace the bulk cold molecular gas, as it is highly abundant and easily detectable at typical molecular cloud densities and temperatures (A. D. Bolatto et al. 2013).

This makes understanding the transitions from $C^+/C/CO$ and $H^+/H/H_2$ crucial for defining where we can trace $H_2$ using CO. These two transitions are not fundamentally at the same spatial location in a PDR, due to differences in shielding mechanisms. $H_2$ is able to self-shield via the Lyman–Werner bands (M. G. Wolfire et al. 2010; N. Y. Gnedin & B. T. Draine 2014), while the C/CO transition is primarily governed by dust shielding and occurs at higher $A_V$, deeper in the PDR. Processes like CO self-shielding and mutual $H_2$/CO shielding can also contribute to the survival of CO (E. F. van Dishoeck & J. H. Black 1988).

In low-metallicity environments, the separation between the $H/H_2$ and $C^+/C/CO$ transitions is expected to increase. This is a consequence of the dust-to-gas ratio dropping with metallicity (A. Rémy-Ruyer et al. 2014; J. Roman-Duval et al. 2022), resulting in lower dust extinction relative to the column density of hydrogen ($A_V/N_H$), allowing FUV photons to penetrate deeper into the cloud (M. G. Wolfire et al. 2010; K. E. Jameson et al. 2018), photodissociating CO, while $H_2$ is protected by self-shielding. As a result, low-metallicity PDRs tend to have larger extents for the same $A_V$ (A. D. Bolatto et al. 2013; A. K. Leroy et al. 2011), causing a larger separation in the chemical transitions. Notably, the shielding of CO by dust is expected to only occur for $A_V \gtrsim 2$ (E. F. van Dishoeck &

J. H. Black 1988; A. Sternberg & A. Dalgarno 1995; R. J. Smith et al. 2014; S. C. O. Glover & P. C. Clark 2016).

Due to the larger separations in the locations of the $H/H_2$ and the $C^+/C/CO$ transition at low metallicity, a significant portion of the $H_2$ mass resides in the "CO-dark" region (where the carbon is either $C^+$ or C) relative to the CO-bright region (T. A. Bell et al. 2007; M. G. Wolfire et al. 2010; S. C. Madden et al. 2020; T. G. Bisbas et al. 2024). Studies of the Small Magellanic Cloud (SMC) point to almost 80% of the $H_2$ mass being in the CO-dark phase (F. P. Israel 1997; A. D. Bolatto et al. 2011; A. K. Leroy et al. 2011; J. L. Pineda et al. 2017; K. E. Jameson et al. 2018), compared to only around 30% in the Milky Way (I. A. Grenier et al. 2005; J. L. Pineda et al. 2013). This results in a metallicity-dependent $X_{CO}$ conversion factor for unresolved clouds, which accounts for the large amounts of CO-dark $H_2$ observed in low-metallicity environments (A. D. Bolatto et al. 2013; M. Gong et al. 2020; S. C. Madden et al. 2020). Given that star formation earlier in the history of the Universe occurred in low-metallicity gas, this metallicity dependence could greatly impact our understanding of high-$z$ observations. Though crucial to studies of ISM physics, resolved predictions of low-metallicity PDR models have never been directly tested due to a lack of observations that can resolve each of the individual boundaries of a PDR. Resolving a low-metallicity PDR will therefore shed light on the CO-to-$H_2$ conversion factor metallicity dependence in other low-metallicity environments such as those in the high-redshift Universe.

Prior to JWST, it was not possible to resolve PDR structures in extragalactic PDRs, particularly the $H/H_2$ transition (as traced by rovibrational $H_2$ emission), due to limits of angular resolution in the near- and mid-infrared. In the Milky Way, to resolve the layers of a PDR, it is essential to reach typical scales of a few $10^{-3}$ pc (C. Joblin et al. 2018; PDRs4AllTeam et al. 2022). While this resolution is still out of reach with JWST anywhere but the Milky Way, the predicted larger spatial extent of PDRs at low metallicity means it is now possible to resolve PDRs in the SMC, at a distance of 62 kpc ($1'' = 0.3$ pc; V. Scowcroft et al. 2016) and metallicity of $0.2\ Z_\odot$ (L. Toribio San Cipriano et al. 2017). The capabilities of JWST and ALMA therefore enable, for the first time, resolving low-metallicity extragalactic PDR structures.

This paper employs JWST and ALMA observations to spatially resolve key PDR transitions in the N13 PDR in the SMC. Using these results, we compare to steady-state plane-parallel PDR models, previously applied to SMC observations (K. E. Jameson et al. 2018), with a set of reasonable assumptions for SMC conditions. In Section 2, we introduce our target and data products. In Section 3, we discuss the creation and analysis of intensity maps and the comparison to PDR models. In Section 4, we analyze the observed PDR structure. In Section 5, we evaluate PDR models and potential influences on the PDR and conclude that the constant-pressure model for N13 aligns best with our observations. In Section 6, we discuss the implications of these results for CO-dark $H_2$.

## 2. Observations and Data Reduction

### 2.1. Target

We investigate a PDR in the N13 region of the SMC located at R.A. $00^h45^m26^s760$, decl. $-73°22'55''66$. The SMC sits at a distance of 62 kpc (V. Scowcroft et al. 2016) and has a
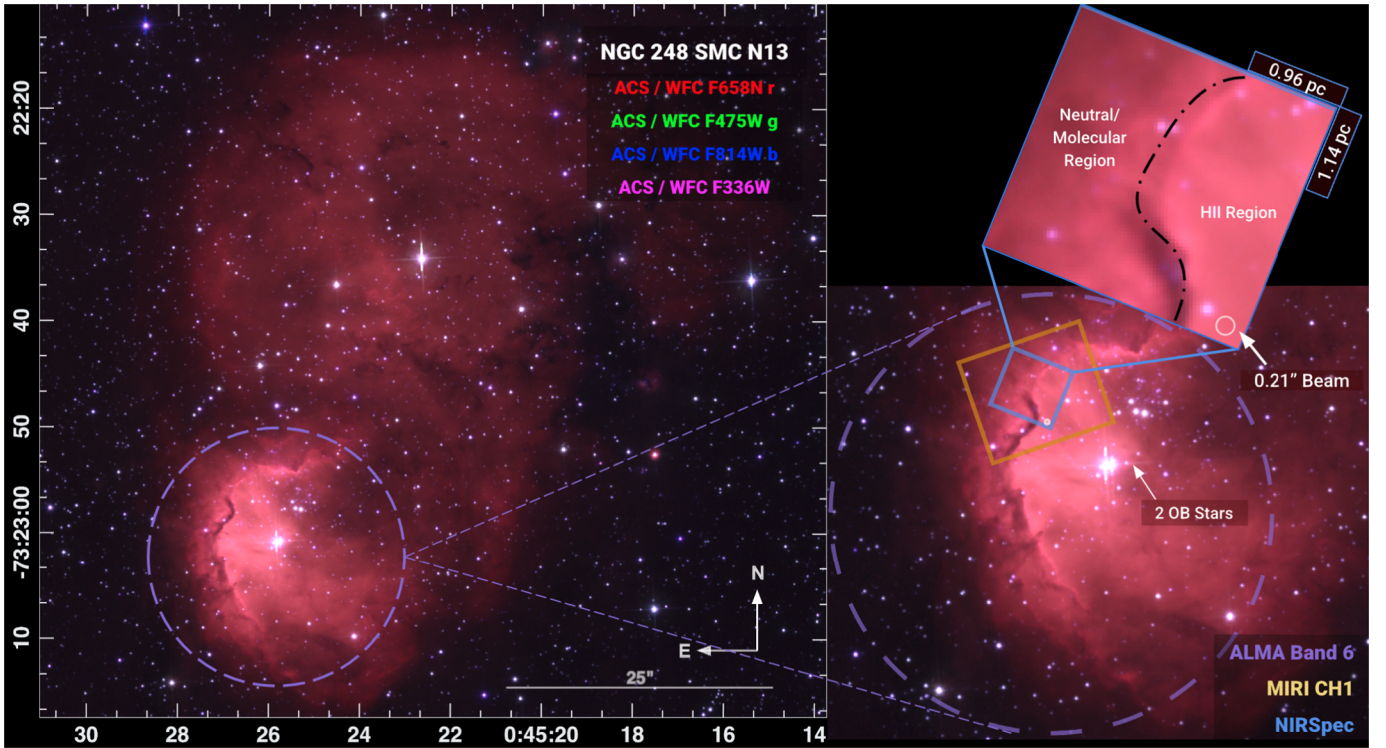
**Figure 1.** In the left panel, we show an HST image of NGC 248, the star-forming region that contains the N13 H II region as seen inside of the purple dashed circle. In the right panel, we show the N13 PDR with the apertures of the different telescope instruments overlaid. This panel also shows a zoom in of the dark edge of the PDR that shows where the molecular gas and dust reside, with a dotted–dashed line giving the approximate by-eye location of the PDR boundary. The two ionizing OB stars that power the N13 PDR are labeled below the apertures. The zoom in on the location of the NIRSpec aperture shows the subparsec-scale spatial resolution we achieve with JWST and ALMA.

subsolar metallicity of $Z = 0.2 \, Z_\odot$ with no systematic gradients across the galaxy (L. Toribio San Cipriano et al. 2017). N13 is a useful laboratory to explore the effects of a low-metallicity environment on the gas and dust properties due to a simple stellar population of two OB stars, similar to the Orion Bar. We selected the region based on the appearance of an edge-on geometry for the PDR in narrowband Hα observations from the Hubble Space Telescope (HST; P. Yanchulova Merica-Jones et al. 2017). Edge-on geometry maximizes the angular separation of the layers to avoid blending and allows for precise spatial identifications of each layer. The geometry appears simple from HST imaging, but we investigate potential inclination effects in Section 5.3. At the distance of the SMC, for an edge-on PDR, we can resolve each PDR layer at spatial resolutions between 0.03 and 0.21 pc with the JWST NIRSpec and MIRI medium-resolution spectroscopy (MRS) integral field unit (IFU) resolution between 0″.1 and 0″.7. On the left side of Figure 1, we show N13 in three HST filters, described in the top-right corner (P. Yanchulova Merica-Jones et al. 2017). We present a zoom in of the N13 PDR on the right side of Figure 1, which is located within the purple dashed circle. The right side of Figure 1 also shows the field of view of the JWST and ALMA observations.

### 2.2. JWST NIRSpec Integral Field Spectroscopy

We observed the N13 PDR using JWST NIRSpec (T. Böker et al. 2022; P. Jakobsen et al. 2022) and MIRI MRS (I. Argyriou et al. 2023) IFUs as part of program GO 2521 in JWST Cycle 1. NIRSpec observations were conducted on 2023 July 29, and MIRI MRS on 2023 July 21. Both NIRSpec and MIRI MRS

used one pointing with four dithers to sample the point-spread function (PSF). For NIRSpec, a "leakcal" was taken for each dither to mitigate MSA slit leakage, while MIRI MRS included "off" observations to remove foreground contamination and pixel-based residuals. We used three NIRSpec medium-resolution gratings (G140M/F070LP, G235M/F170LP, G395M/F290LP), and all MIRI MRS channels and gratings spanning 5–28 μm. In the following, we present results using the higher-spatial-resolution observations from NIRSpec to dissect the PDR. A description of the MIRI MRS observations and their analysis will be presented in a future paper.

Data were downloaded from MAST and reduced using the JWST pipeline. For NIRSpec, we used a development version of the pipeline that allowed for $1/f$ noise removal from both the "on" and "leakcal" observations (JWST pipeline version 1.16.1.dev14; H. Bushouse et al. 2024) using CRDS `jwst_1293.pmap`. We processed the raw `uncal` files through the Detector1 pipeline, including $1/f$ noise correction with the `clean_flicker_noise` step. We then ran the Spec2 and Spec3 pipeline stages and created a drizzled cube with 0″.05 pixels for each grating. Typical uncertainties per spaxel in the cubes range from 0.3 to 0.5 MJy sr$^{-1}$ for G140M and G235M and 0.3–1 MJy sr$^{-1}$ for G395M.

#### 2.2.1. Astrometric Alignment

Given the subparsec-scale separations we aim to measure in the PDR, ensuring accurate astrometry is critical. The astrometry of the ALMA observations is well understood due to the nature of interferometric measurements with extragalactic radio sources as phase calibrators. The astrometry of the JWST

observations, however, can have offsets related to uncertainty in the positions of guide stars.

To correct the JWST astrometry, we compared to archival data from HST (P. Yanchulova Merica-Jones et al. 2017) in the Advanced Camera for Surveys/Wide Field Camera F475W filter, which we aligned to Gaia Data Release 3 (DR3; HST has similar astrometric uncertainties related to guide stars, but a much larger field of view than the JWST IFUs). We found 1000 Gaia DR3 catalog stars within the HST field to use as our astrometric reference. Using the photutils.centroids Python package (L. Bradley et al. 2023), we measured the centroid positions of these stars in the HST F475W image and computed average offsets in R.A. and decl. to find the overall astrometric shift in the HST data. We find a Gaia–HST offset in R.A. of $-0\rlap{.}{''}174 \pm 0\rlap{.}{''}039$ and in decl. of $0\rlap{.}{''}158 \pm 0\rlap{.}{''}010$m where the errors are the standard deviation over the 1000 Gaia DR3 stars.

We then identify four stars within the NIRSpec G140M cube that are also evident in the HST imaging and use these to correct the JWST astrometry, using the same centroid and averaging method as described above. We find an HST–JWST offset in R.A. of $-0\rlap{.}{''}444 \pm 0\rlap{.}{''}022$ and in decl. of $-0\rlap{.}{''}197 \pm 0\rlap{.}{''}011$, where the error listed here is the standard deviation of the offsets. To check our astrometric correction, we compared Gaia astrometry-corrected HST data with the ALMA $^{12}$CO $J = 2-1$ moment-zero map. The alignment between the CO emission and the dust lane in the HST image matched well, giving us confidence that the JWST-HST-ALMA alignment was robust.

### 2.2.2. Integrated Line Maps from JWST

To measure the integrated intensity of spectral lines in the JWST spectral cubes, we used two different approaches based on the line's intensity, the complexity of decomposing its emission from surrounding PAH features, and potentially blended spectral lines. For H recombination lines, and the 3.3 $\mu$m PAH emission feature, we used the Python implementation of the PAHFIT package (J. D. T. Smith et al. 2007).[18] This model works well for PAH features and for bright and/or blended emission lines. For fainter lines, like the $H_2$ $1-0$ S(1) 2.12 $\mu$m vibrational line, errors in the local PAHFIT continuum fitting can be significant, so we instead do a local continuum fit and integrate under the line. In this case, we defined continuum regions around each line, fit a one-dimensional polynomial, and then subtracted the fitted continuum before integrating under the line.

We fit emission lines and PAH features in each spaxel and created maps of the integrated feature strengths. We applied the fitting to all spaxels in the NIRSpec cubes. We created resolved integrated intensity maps for key lines such as the 2.12 $\mu$m $H_2$ $1-0$ S(1), 4.05 $\mu$m H I $5-4$ Brackett $\alpha$ (Br$\alpha$), 1.87 $\mu$m H I $4-3$ Paschen $\alpha$ (Pa$\alpha$), and the 3.3 $\mu$m PAH feature. We calculate signal-to-noise ratio (S/N) values at the first peak of the radial profiles (discussed in Section 4.2) to be $\sim$58 for $H_2$ 2.12 $\mu$m, $\sim$179 for H I $4-3$ Pa$\alpha$, $\sim$87 for H I $5-4$ Br$\alpha$, and $\sim$29 for the 3.3 $\mu$m PAH feature. We also use archival data from HST F658N narrowband photometry, obtained from P. Yanchulova Merica-Jones et al. (2017), to trace H$\alpha$. Figure 2 shows the resulting line and PAH maps for N13. Further analysis of these maps is provided in Section 4.1.

### 2.3. ALMA

We obtained data for $^{12}$CO $J = 2-1$ in Band 6, $^{12}$CO $J = 3-2$ in Band 7, and [C I] $^3P_1$-$^3P_0$ $1-0$ in Band 8 using the ALMA 12 m array and Atacama Compact Array (ACA) 7 m array in Project ID 2021.1.01065.S. The target angular resolution of $0\rlap{.}{''}25$ (0.075 pc) was set to resolve the PDR layers given predictions from PDR models described in Section 3.2. We observed a single pointing for all ALMA observations, as the PDR is smaller than the field of view in all bands. The 12 m and 7 m configurations included in each observation were set to recover angular scales up to at least $15''$, which covers the angular extent of the molecular cloud in N13 detected in previous observations (H. P. Saldaño et al. 2024) and is larger than the JWST field of view.[19] We did not observe the $^{12}$CO $J = 1-0$ line due to low surface brightness with the extended configuration necessary to reach $0\rlap{.}{''}25$ resolution. The Bands 6, 7, and 8 observations used 0.09, 0.12, and 0.09 km s$^{-1}$ velocity resolution, significantly higher resolution than the line widths of $\sim$0.5 km s$^{-1}$. The observed bandwidths for Bands 6, 7, and 8 each cover $> 140$ km s$^{-1}$, encompassing the velocity extent of the emission in this portion of the SMC.

We used version 1.0 of the PHANGS-ALMA pipeline (A. K. Leroy et al. 2021)[20] to image the calibrated data from the 12 m array and ACA and generate cubes and moment maps. We convolve all cubes to have circular Gaussian beams, but do not convolve to matched spatial resolution. For our goal of identifying the layers of the PDR, the highest-resolution version of the data is ideal. The final resolution of the cubes are $0\rlap{.}{''}270$ for $^{12}$CO $J = 2-1$, $0\rlap{.}{''}331$ for CO $3-2$, and $0\rlap{.}{''}276$ for [C I] $1-0$. The moment map generation includes a step of signal masking to create high-confidence moment maps, following the "broad" mask procedure in the PHANGS pipeline. In our $^{12}$CO $J = 2-1$, $^{12}$CO $J = 3-2$, and [C I] $1-0$ moment-zero maps, we find rms values of 1.464 K km s$^{-1}$, 1.098 K km s$^{-1}$, and 1.112 K km s$^{-1}$, respectively. We calculate S/N values at the peak of the radial profiles (discussed in Section 4.2) to be $\sim$39 for $^{12}$CO $J = 2-1$, $\sim$56 for $^{12}$CO $J = 3-2$, and $\sim$10 for [C I] $1-0$.

## 3. Methods

We aim to map the spatial structure of the N13 PDR and compare to PDR models in order to determine the separations between the ionization front (IF), dissociation front (DF), and C/CO transition. Observationally, the available tracers are emission lines that emerge from gas at different depths in the PDR. While it is possible to select tracers that should have distinct spatial profiles across PDR boundaries (e.g., peaks or drops), we are limited by the angular resolution of our observational data set and by the lack of direct observables for the abundances of the relevant species. In order to compare to models, we use the volume emissivity of the relevant emission lines, which translates the abundance and temperature profiles of the PDR models into "observable" space. We further

---

[18] https://github.com/PAHFIT/pahfit

[19] At present, the second 12 m configuration for the Band 8 [C I] observations has not been observed. Using the full Band 8 data set for CO $J = 3-2$, which has the same set of configurations, we tested the effect of the missing 12 m configuration on the location of the peak in the PDR and did not see any significant differences. The lack of 12 m data yields lower than planned S/N, but does not affect the observed peak location, which is the focus of this paper.
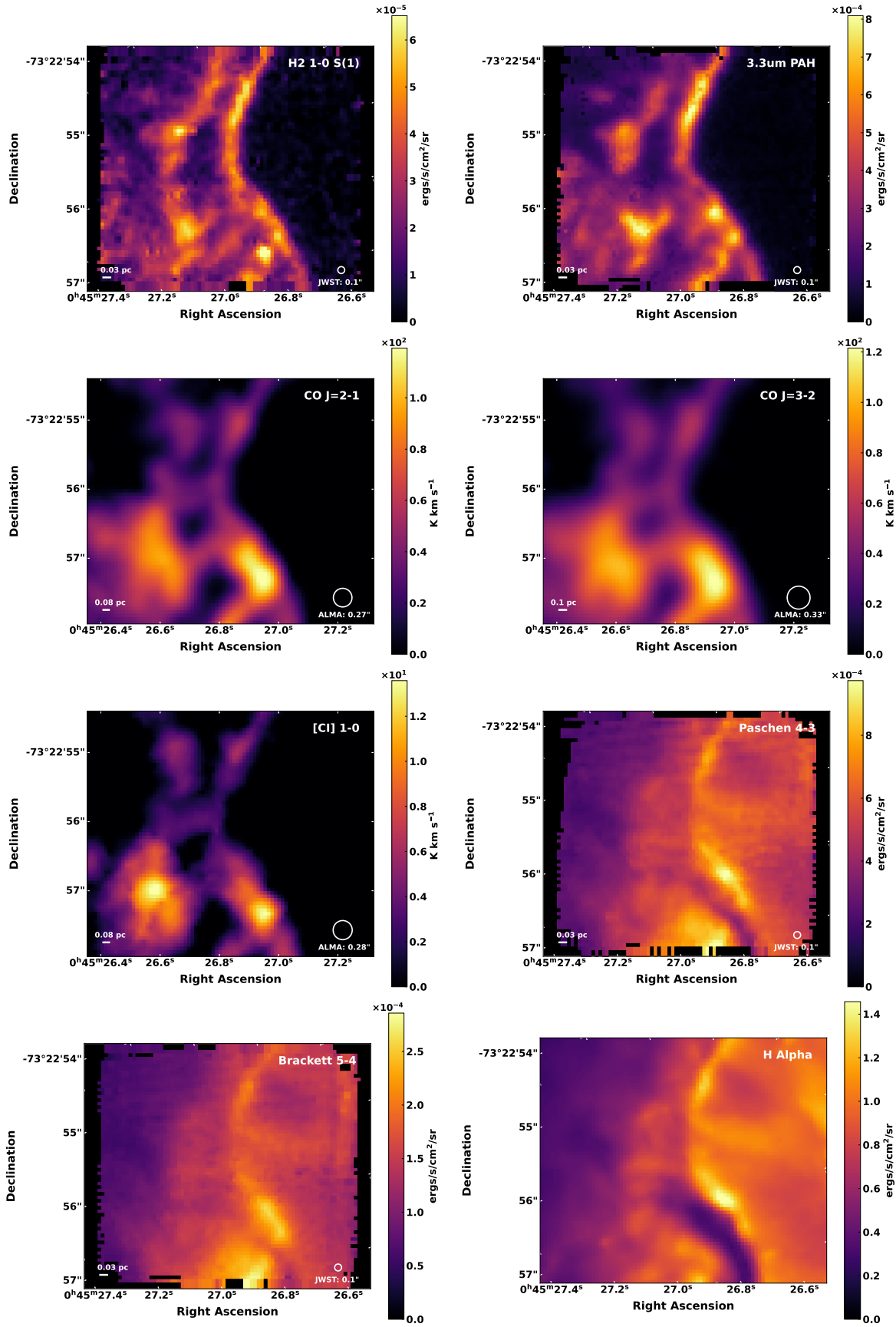[20] The PHANGS-ALMA pipeline can be found at https://github.com/akleroy/phangs_imaging_scripts.

**Figure 2.** Integrated intensity maps for the $H_2$ 2.12 $\mu$m line, the 3.3 $\mu$m PAH feature, H I 4–3 Paschen $\alpha$, H I 5–4 Brackett $\alpha$, and the moment-zero maps of $^{12}$CO $J = 2-1$, $^{12}$CO $J = 3-2$, and [C I] 1–0. We also show the F658N HST filter for reference, as we use this map for the H$\alpha$ radial profile discussed in Section 4.2. The structure of the PDR is well resolved in all of the tracers, showing two dissociation fronts (DFs) and a filamentary structure.

convolve each model emissivity profile to match the angular resolution of the corresponding observed emission line. This allows us to locate the emission peaks in both models and observations for each relevant tracer to identify the PDR boundaries.

The emission lines we use to compare the observations and models include H I Paα 1.87 $\mu$m, which should show a decrease in emission after the IF; $H_2$ 1–0 S(1) 2.12 $\mu$m, which should peak near the DF; and [C I] $^3P_1$-$^3P_0$ 609 $\mu$m, $^{12}CO$ $J = 2 -1$, and $^{12}CO$ $J = 3-2$, which should trace the transition from C to CO. The correspondence between emission profiles and the expected location of the PDR boundaries is discussed in Section 4.1. We create radial profiles to characterize each key tracer map, as described in Section 3.1.

Our comparison PDR models are tailored for SMC conditions and anchored to the density and/or pressure observed in the nearby H II region, as described in Section 3.2. In identifying the best-matched model to our observations, we allow for small changes in density and pressure in the models, within their uncertainties, and select the model that provides the closest match to the observed peak spacings between the DF and the C/CO transition. We align model-predicted peak locations with our observations rather than doing a formal fit of the models. A formal fitting procedure is not warranted given the limited comparison (DF to C and DF to CO peak locations) and the large number of additional model parameters. Translating PDR models to observables via the volume emissivities is a standard way to compare the location of emission peaks from edge-on models with observations (e.g., C. Joblin et al. 2018; J. R. Goicoechea et al. 2019). The calculation of model intensities would depend on additional considerations such as the angle of the line of sight and optical depth effects in the line. Our approach enables a matched-resolution comparison of the spatial separation between the DF and the C/CO transition, allowing us to evaluate how well the models reproduce the observed low-metallicity structure. In doing this comparison between modeled and observed boundary separations between peaks, we characterize N13's PDR structure and the extent of CO-dark $H_2$ content between the DF and the C/CO boundary. We step through this process in more detail below.

### 3.1. Radial Profile Analysis

To analyze the spatial separation of the PDR boundaries of N13, we generated radial profiles along a slice perpendicular to the PDR. We selected the end coordinates of a perpendicular slice by visual inspection using the CARTA software package (A. Comrie et al. 2021). This slice was selected to be as perpendicular as possible to the PDR $H_2$ emission to yield a clean, simple radial profile. We chose this particular placement of the slice to avoid complex structure from an embedded young stellar object (YSO) in the south and to have enough coverage for the profile to not extend past the edge of the cube in the north. We find this location of the slice to produce profiles that have a clear peak for PDR boundary analysis for all of the maps analyzed.

We measured the integrated intensity of $H_2$ 2.12 $\mu$m, CO $J = 2 -1$, CO $J = 3-2$, and [C I] 1−0 emission along the slice with a step size of 0″.01, which oversamples the resolution elements of JWST and ALMA. We used the griddata cubic interpolation method to measure the intensities at each point of the slice. In Figure 3, we show the main perpendicular slice in blue. We provide the radial profile measurements for each map in Tables 2

and 3. The parallel dashed blue lines represent additional slices, offset by the pixel scale, used to estimate uncertainties in the peak spatial placement. It is important to note that the OB stars powering N13 are not the starting point of the slice. The primary goal of the slice is to locate the different peaks from each PDR tracer and measure their separations relative to each other. In Figure 4, the $x$-axis of the profiles increases away from the OB stars, where zero marks the point closest to the stars (5″.992, or 1.81 pc pc away from the OB stars).

### 3.2. PDR Models

The density distribution of the gas is one of the main parameters in PDR modeling. Many PDR models use constant-density, plane-parallel, semi-infinite slabs of gas and dust to model observations (e.g., A. G. G. M. Tielens & D. Hollenbach 1985). While constant-density plane-parallel models can successfully describe line intensities and the spatial separation of layers in some PDRs, there are several processes that can modify this picture. Constant-thermal-pressure models tend to increase the density in the deeper (cooler) layers and lead to a convergence of layers (C. Joblin et al. 2018). Density inhomogeneities like high-density clumps, produced by compression from turbulence (S. C. O. Glover & M. M. Mac Low 2011) or photoevaporation (U. Gorti & D. Hollenbach 2002), can lead to spatially unresolved H/$H_2$ and $C^+$/C/CO transitions surrounding the denser clumps. Photoevaporation from the PDR surface into the H II region can lead to an advection flow that draws the $H_2$ and C/CO layers toward the IF, leading to a convergence of layers (H. Störzer & D. Hollenbach 1998; E. Bron et al. 2018; V. Maillard et al. 2021). Endoergic carbon chemistry, overcome by FUV-pumped, excited $H_2$, can produce carbon species such as CO and $HCO^+$ coincident with the $H_2$ (A. Sternberg & A. Dalgarno 1995; J. R. Goicoechea et al. 2016), also leading to overlapping $H_2$ and C/CO layers. The plane-parallel (steady-state) model is a more simplistic geometry for PDR structure, but may still provide a reasonably good fit for some PDRs.

Differences between the plane-parallel and clumpy models mainly hinge on the surface-to-volume ratio of the model PDR. Future efforts may be able to model three-dimensional PDR structures from simulated molecular clouds (T. G. Bisbas et al. 2012) or use models that directly couple the hydrodynamics and chemistry (S. C. O. Glover & P. C. Clark 2012; T. Grassi et al. 2014; T. G. Bisbas et al. 2015; D. Seifried et al. 2017; A. Lupi et al. 2018; S. Haid et al. 2019; D. Seifried et al. 2020; E. Bellomi et al. 2020; C.-Y. Hu et al. 2021; B. A. L. Gaches et al. 2023; A. Gurman et al. 2024; see also the review by M. G. Wolfire et al. 2022).

Currently, it is not clear that low-metallicity PDRs would necessarily be preferentially isobaric (constant pressure), isochoric (constant density), or clumpy. However, we can now test different model predictions for the C/CO transition in the low-metallicity environment of the SMC. It is important to note that in models which have a fixed level of turbulence, along with a fixed radiation field spectrum and intensity and cosmic-ray rate, a low-metallicity cloud tends to be less clumpy than a high-metallicity one (S. C. O. Glover & M. M. Mac Low 2011). This difference is primarily due to higher temperatures and lower turbulent Mach numbers at low metallicity. However, because there are still density substructures that form at low metallicities, we cannot necessarily conclude that clumpy models are not appropriate for low-metallicity clouds.
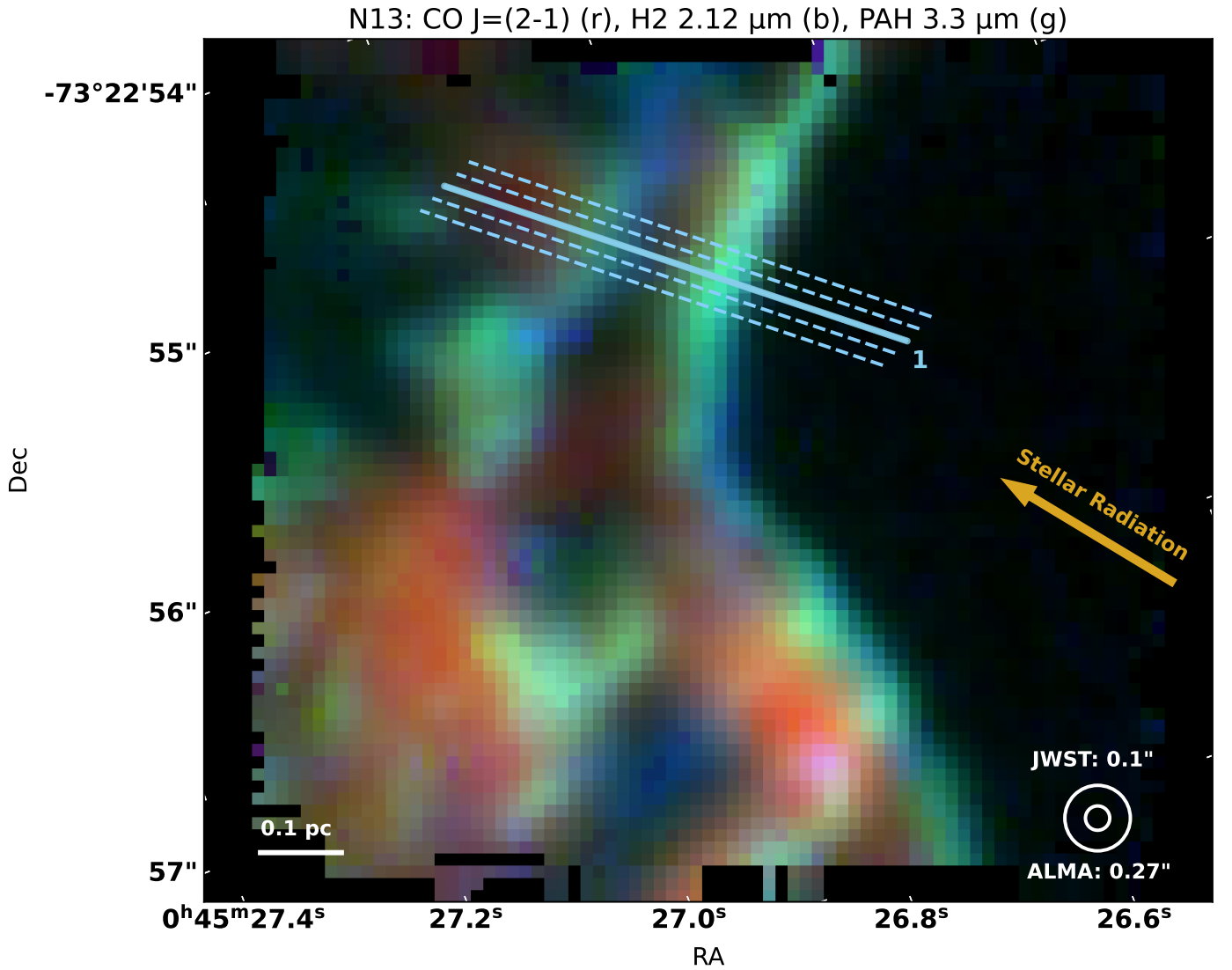
**Figure 3.** Three-color image of the N13 PDR, with $H_2$ 2.12 $\mu$m in blue, CO $J = 2-1$ in red, and the 3.3 $\mu$m PAH feature in green. We show our main radial line profile in blue, labeled as "1", interpolated at 0″.01 spacing. The dashed blue lines indicate the additional slices used to calculate uncertainty, separated by the pixel scale. The starting coordinates for each slice are in the H II region, closer to the illuminating stars located to the right of the map. The radial profiles are discussed further in Section 3.1.

To analyze our observations, we use our PDR model based on that of A. G. G. M. Tielens & D. Hollenbach (1985) with updates to the dominant chemistry and thermal processes given in M. J. Kaufman et al. (2006), M. G. Wolfire et al. (2010), D. Hollenbach et al. (2012), and D. A. Neufeld & M. G. Wolfire (2016), and tailored for the SMC as in K. E. Jameson et al. (2018). These are plane-parallel models of a layer of gas and dust exposed to a FUV radiation field with a fixed spectral shape and a cosmic-ray flux.[21] The abundances of the atomic and molecular species as a function of depth into the cloud are found from steady-state chemical balance, and the gas temperature from thermal equilibrium (see, e.g., V. Maillard et al. 2021, for an exploration of nonsteady state models at low metallicity). We use a primary cosmic-ray ionization per H of $3.3 \times 10^{-17}$ s$^{-1}$ H$^{-1}$ estimated from scaling the local Galactic

value from D. A. Neufeld & M. G. Wolfire (2017) by a factor 0.15 for the reduced density of cosmic rays in the SMC measured by Fermi (A. A. Abdo et al. 2010), assumed to be homogeneous along the line of sight through the PDR. The assumed dust and metal abundances are customized for the N13 PDR in the SMC. We use gas-phase abundances of metals that are one-fifth of the local Galactic values (L. Toribio San Cipriano et al. 2017), $A_V/N_H = 5.35 \times 10^{-23}$ cm$^2$ from K. D. Gordon et al. (2024), a small grain abundance of 1/7.7 of the Galactic value from K. M. Sandstrom et al. (2010), and an appropriate FUV extinction curve (K. D. Gordon et al. 2003, 2024), resulting in a factor of 2 higher FUV opacity in the photo rates compared to those listed in A. N. Heays et al. (2017) for the Galactic case (see also K. E. Jameson et al. 2018 and the Appendix for additional model details). Additional studies of PDRs at low metallicity include M. J. Kaufman et al. (2006), M. Röllig et al. (2006), S. Bialy & A. Sternberg (2019), and T. G. Bisbas et al. (2021, 2025).

We estimated $G_0$ from the massive star that dominates the ionizing photon production rate in N13, which is equivalent to

---

[21] The use of a fixed spectral shape is justified because $H_2$ and CO share the same narrow photodissociation wavelength band (E. F. van Dishoeck & J. H. Black 1988), implying that their photo-processes scale similarly with an increase in FUV flux.
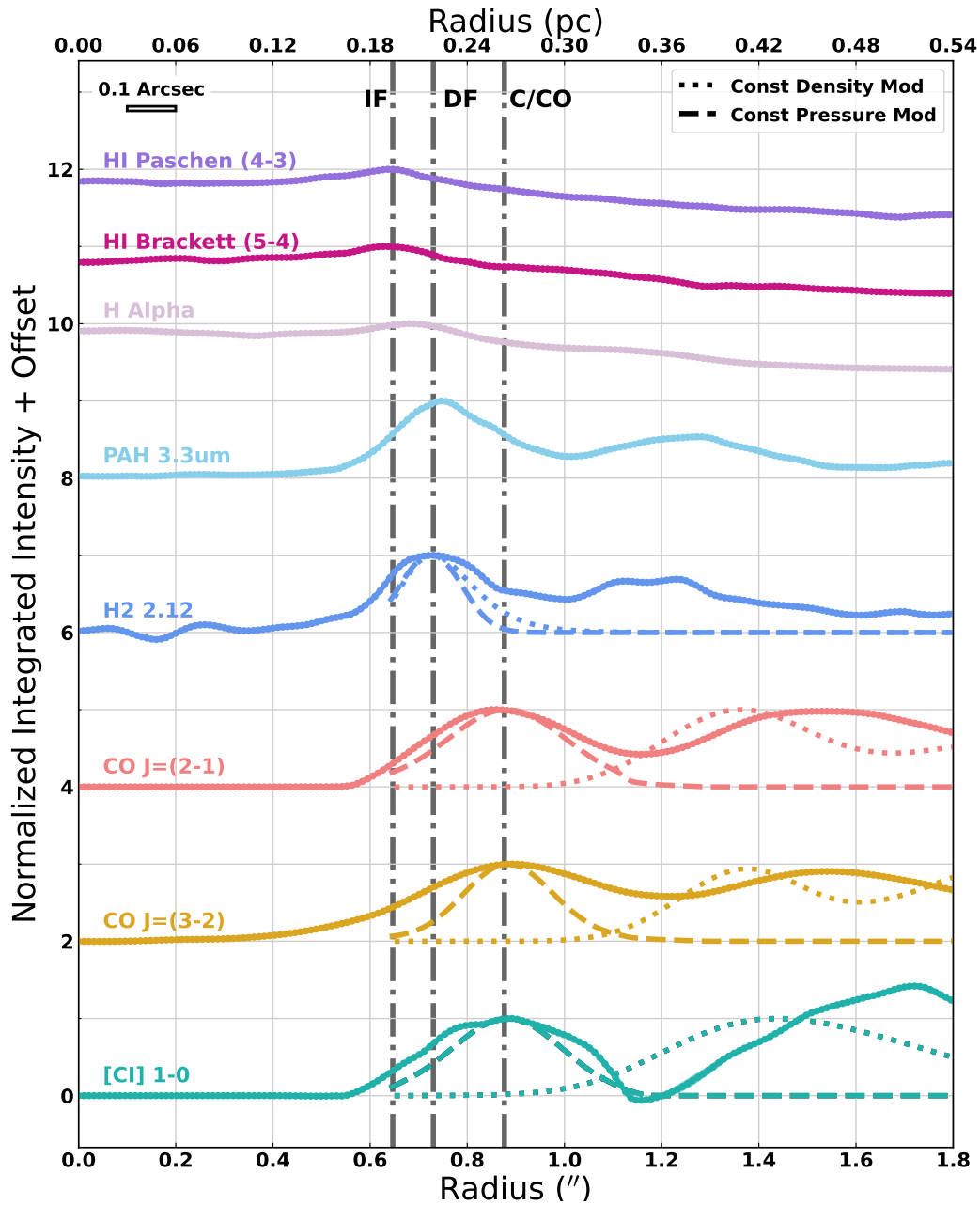
**Figure 4.** We present the stacked and normalized linear radial profiles of the integrated intensity maps of H I 4–3 Paschen $\alpha$, H I 5–4 Brackett $\alpha$, H$\alpha$ from HST F658N photometry, the 3.3 $\mu$m PAH feature, H$_2$ 2.12 $\mu$m, $^{12}$CO $J = 2-1$, $^{12}$CO $J = 3-2$, and [C I] 1–0. We observe a peak in the H I Paschen 4–3 profile before the dissociation front (DF), followed by a subsequent decline, which we interpret as the ionization front (IF). We identify the IF, the DF, and the C/CO transition, from left to right, as seen in the vertical dashed–dotted gray lines in each panel. We also present the stacked and normalized linear radial emissivity profiles, convolved for each beam, of the $P_{th}/k = 7.6 \times 10^6$ K cm$^{-3}$ constant-pressure (dashed) and $n = 3.9 \times 10^4$ cm$^{-3}$ constant-density (dotted) models, which are color-coded to match the observed profiles.

an O7 star of $T_{eff} \sim 38$ kK (V. Ramachandran et al. 2019), and use the FUV luminosity of a Galactic star of the same $T_{eff}$, $L_{FUV} = 1.6 \times 10^5 L_\odot$ (A. Parravano et al. 2003; P. S. Conti et al. 2008), and a distance of 1.8 pc from the star to PDR boundary. This yields $G_0 \sim 10^3$ in units of the Habing field ($1.6 \times 10^{-3}$ erg cm$^{-2}$ s$^{-1}$; H. J. Habing 1968).[22] We test models of constant density $n$, and constant thermal pressure $P_{th}/k$, where $n$ is the density of hydrogen nuclei and $k$ is the

Boltzmann constant. These correspond to the limiting cases of a cloud completely dominated by magnetic pressure so that $T$ drops without changing the density, and a cloud in which the magnetic pressure is negligible. We use a thermal pressure $P_{th}/k \sim 7.6 \times 10^6$ K cm$^{-3}$, which provides the best match to the observed separation between the DF and CI/CO peaks by minimizing the distance between the model and the observed peaks (see Section 5.1).

With this pressure, our PDR model gives a density of $n \sim 3.9 \times 10^4$ cm$^{-3}$ at the cloud edge, which we use as our constant-density model since it ensures pressure balance between the H II region and the PDR (see, e.g., the analysis in Y. M. Seo et al. 2019). In contrast to the constant-pressure

---

[22] This assumes the minimum distance between the PDR and star and gives an upper limit to $G_0$. The field can be lower if the star is substantially in the foreground or background, however the spherical appearance of the N13 region suggests this distance is reasonable.

case, we do not force the constant-density model to match the observed peak separation. Matching the constant-density peak separations would require a pressure 7 times higher than what is observed in the H II region, making it physically unrealistic. We note that future, more detailed studies with JWST observations will refine these numbers. For the present effort, the models are used for comparison with the observed locations of the IF, DF, and C/CO transitions as shown at the bottom of Figure 4, colored by emission line. In Figure 4, we plot both the constant-density (dotted) and the constant-pressure (dashed–dotted) models along with each corresponding radial profile for the emission as discussed in Section 4.

## 4. Results

### 4.1. Observed Structure of N13

To quantify the structure of the PDR, we use the radial profiles to find the locations of the peak intensity of various emission lines, related to the IF, DF, and C/CO transition. We then compare these measurements to line intensities from PDR models.

To locate the DF in the N13 PDR, we used the $H_2$ 2.12 $\mu$m vibrational line, which is a good indicator of the H I to $H_2$ transition (see the Appendix). This line is the 1–0 vibrational transition and is, therefore, the last vibrational transition in the $H_2$ fluorescent cascade, making it one of the strongest $H_2$ lines in the NIRSpec wavelength range, and a key marker for identifying the DF (see E. Peeters et al. 2024, for the same measurement in the Orion Bar PDR).

Our radial profiles of the $H_2$ 2.12 $\mu$m 1–0 S(1) line, shown in Figure 4, reveal two distinct intensity peaks that we interpret as two separate DFs. Similar multiple DF structures have been observed in the Orion Bar (E. Peeters et al. 2024). Our analysis will focus on the first "primary" DF in all subsequent discussions. The second DF also exhibits a similar structure to the first DF. To understand the nature of the $H_2$ emission generating the observed peak, we create a map of the $H_2$ 2.24 $\mu$m 2−1 S(1) line, and generate a corresponding radial profile for comparison against the $H_2$ 2.12 $\mu$m emission. We analyze the ratio of the 1–0 S(1) to 2−1 S(1) intensities at the first peak of the $H_2$ 1–0 S(1) radial profile, located at 0″73. At this position, we measure a 1–0 S(1)/2−1 S(1) ratio of 2.17, characteristic of a primarily $H_2$ FUV-pumped region. In the Orion Bar, E. Peeters et al. (2024) find similar $H_2$ $v = 1$–0 S(1)/$v = 2$−1 S(1) line intensity ratios of $\sim$ 3–5 in each of the three different DFs. We also find that the structure of the $H_2$ 2.12 $\mu$m and 3.3 $\mu$m PAH radial profiles look strikingly similar, in contrast to the Orion Bar PDR, where the PAH emission peaks at the IF and is bright in the atomic gas region (E. Peeters et al. 2024). We also observed two peaks in the PAH feature integrated intensity radial profile.

With the Pa$\alpha$ and Br$\alpha$ line maps, we explore the location of the IF. We look for a decline in H I recombination line intensities that corresponds to the edge of the H II region. This location marks the transition from H$^+$ to H. We compare the H I recombination lines to the $H_2$ 2.12 $\mu$m, CO, and [C I] emission in Figure 4. We observe the ionized gas to be more extended but do observe a peak, and a subsequent dip, right before the DF, which we interpret as the IF. We measure the IF as the peak in the H I Pa$\alpha$ 4–3 line to sit at 0″647 $\pm$ 0″060, or 0.195 $\pm$ 0.013 pc, from the arbitrary zero-point of the radial profile.

We attempt to measure the location of the C/CO transition using the ALMA maps ($^{12}$CO $J = 2$−1, $^{12}$CO $J = 3$−2, and [C I] 1–0). However, as is evident in Figure 2, the [C I] and CO exhibit similar structures. The small separations between CO and [C I] emission could be taken as a signature of clumpiness in the PDR, where in unresolved cases, clumps make it appear that both CO and [C I] are cospatial (A. D. Bolatto et al. 1999; M. Röllig et al. 2006; S. C. O. Glover & P. C. Clark 2016; N. Izumi et al. 2021). However, this small overlap could also be consistent with a constant-pressure model where density increases in the cooler, shielded gas, leading to a convergence of the [C I] and CO layers below our resolution, a topic we discuss further in Sections 5.1 and 5.4. Because the separations between the $^{12}$CO $J = 2$−1, $^{12}$CO $J = 3$−2, and [C I] 1−0 layers are unresolved, we quote an upper limit on their spacing and use the average position of the peak in $^{12}$CO $J = 2$−1 and $^{12}$CO $J = 3$−2 to define the boundary of the C/CO transition in Section 4.2. We note that the location of the peak in CO emission is very close to, but is not exactly located at, the C/CO boundary determined from C and CO modeled abundances, as shown in the Appendix.

We note that we also observe CO ice absorption near the first DF (R.A. 00:45:26.794, decl. −73:22:57.697), indicating the presence of an embedded YSO. This position is not near our radial profile, so does not affect our measurements of the PDR layer spacings.

### 4.2. Distances between PDR Boundaries

A key goal of this study is to resolve the PDR boundaries in a low-metallicity environment. In Figure 4, we overplot and normalize the radial profiles to the peak value of each emission line over the whole profile. We also show the convolved constant-pressure (dashed) and constant-density (dotted) models for the $H_2$ 2.12 $\mu$m, [C I] 1–0, $^{12}$CO $J = 2$−1, and $^{12}$CO $J = 3$−2 lines. We label the IF, DF, and the C/CO boundary on each of the plots in vertical gray dashed–dotted lines. We also present the ionized gas tracers H I Pa$\alpha$, Br$\alpha$, and H$\alpha$, which are not included in the models. To compare to the PDR models, we make the same measurements on the modeled line emissivity to characterize the separations, convolving each model tracer to match the corresponding resolution of each observed emission line. We note that comparing model emissivities with observables is typical for edge-on PDRs (C. Joblin et al. 2018; J. R. Goicoechea et al. 2019), but the absolute line intensities depend on the viewing angle. The emissivity and intensity profiles could be different in the case of opacity effects, especially for the CO lines. However, we find that the emissivity peaks close to the edge of where the CO abundance starts to rise, where the gas temperatures and densities are sufficiently high to excited the lines.

Figure 4 demonstrates that we have measured the separation between the DF and the peaks in [C I] and CO emission, indicating we have resolved the PDR structure. Table 1 lists the locations and separations for the $H_2$ 2.12 $\mu$m, [C I] 1−0, $^{12}$CO $J = 2$−1, $^{12}$CO $J = 3$−2, H I Pa$\alpha$, H I Br$\alpha$, and H$\alpha$ lines, with distances converted to parsecs using the SMC distance of 62 kpc (V. Scowcroft et al. 2016). We also present the separations measured from the constant-density/pressure models. We take the location of the C/CO transition to be the average of the $^{12}$CO $J = 2$−1 and $^{12}$CO $J = 3$−2. We give an upper limit on the separation between $^{12}$CO $J = 2$−1 and [C I] 1−0 as they are not distinguished within their respective

**Table 1**
Key Locations and Separations of PDR Layers

| Radial Slice Locations | | |
| --- | --- | --- |
| | R.A. (hh:mm:ss) | Decl. (deg:arcmin:arcsec) |
| Start coordinates | 0: 45: 26.6275 | −73: 22: 56.1209 |
| End coordinates | 0: 45: 26.9911 | −73: 22: 54.8568 |
| **Locations of First Peak** | | |
| Species | Arcsecond ($''$) | Parsec (pc) |
| $H_2$ 2.12 $\mu$m | $0\rlap{.}''730 \pm 0\rlap{.}''040$ | $0.220 \pm 0.013$ |
| 3.3 $\mu$m PAH | $0\rlap{.}''746 \pm 0\rlap{.}''032$ | $0.225 \pm 0.009$ |
| $^{12}CO$ $J = 2-1$ | $0\rlap{.}''860 \pm 0\rlap{.}''011$ | $0.260 \pm 0.003$ |
| [C I] 1–0 | $0\rlap{.}''892 \pm 0\rlap{.}''013$ | $0.270 \pm 0.004$ |
| $^{12}CO$ $J = 3-2$ | $0\rlap{.}''892 \pm 0\rlap{.}''011$ | $0.270 \pm 0.003$ |
| H I Paschen $\alpha$ | $0\rlap{.}''647 \pm 0\rlap{.}''060$ | $0.195 \pm 0.018$ |
| H I Brackett $\alpha$ | $0\rlap{.}''627 \pm 0\rlap{.}''070$ | $0.189 \pm 0.021$ |
| H$\alpha$ | $0\rlap{.}''680 \pm 0\rlap{.}''145$ | $0.205 \pm 0.044$ |
| **PDR Layer Separations** | | |
| Separation Type | Arcsecond ($''$) | Parsec (pc) |
| IF $\rightarrow$ DF | $0\rlap{.}''083 \pm 0\rlap{.}''033$ | $0.025 \pm 0.009$ |
| DF $\rightarrow$ C/CO$_{avg}$ | $0\rlap{.}''146 \pm 0\rlap{.}''042$ | $0.043 \pm 0.013$ |
| $^{12}CO$ $J = 2-1 \rightarrow {}^{12}CO$ $J = 3-2$ | $<0\rlap{.}''032$ | $< 0.009$ |
| $^{12}CO$ $J = 2-1 \rightarrow$[C I] 1–0 | $<0\rlap{.}''032$ | $< 0.009$ |
| Const. density model IF $\rightarrow$ DF | $0\rlap{.}''080$ | $0.024$ |
| Const. density model DF $\rightarrow {}^{12}CO$ $J = 2-1$ | $0\rlap{.}''650$ | $0.195$ |
| Const. density model DF $\rightarrow$ [C I] 1−0 | $0\rlap{.}''710$ | $0.213$ |
| Const. pressure model IF $\rightarrow$ DF | $0\rlap{.}''090$ | $0.027$ |
| Const. pressure model DF $\rightarrow {}^{12}CO$ $J = 2-1$ | $0\rlap{.}''150$ | $0.045$ |
| Const. pressure model DF $\rightarrow$ [C I] 1−0 | $0\rlap{.}''150$ | $0.045$ |

**Note.** R.A. and decl. of profile cuts perpendicular to the PDR as seen on the $H_2$ 2.12 $\mu$m line integrated intensity map (see Figure 2). The beginning points ($0\rlap{.}''0$) are offset from the star by $5\rlap{.}''992$ (1.81 pc). Profiles are sampled at $0\rlap{.}''01$ spacing. We also present the separations in the peak intensities of the radial profiles. We show the separation of the layers in angular arcsecond units ($''$) and parsec (pc) scales. The errors on the peak measurements come from the standard deviation of peak calculations on each of the five slices, as seen in Figure 3. We use the average of the $^{12}CO$ $J = 2-1$ and $^{12}CO$ $J = 3-2$ peaks to define the C/CO transition at $0\rlap{.}''876 \pm 0\rlap{.}''016$, since $^{12}CO$ $J = 2-1$ and [C I] 1−0 are not distinguished within their respective uncertainties. We note that the models of a single, constant-density PDR have two peaks in CO emission, the first of which is used to calculate the model separations.

uncertainties. The separations between the DF, [C I], and CO emission suggest a compact PDR structure, which we compare to models in the following sections.

## 5. Discussion

Our radial profile analysis reveals clear separations between key species in the DF and the C/CO transition. We find the separation between the DF and C/CO to be $0.043 \pm 0.013$(stat.) $\pm 0.0036$ (syst.) pc. The statistical (stat.) error comes from the four adjacent slices around slice 1. The systematic (syst.) error is determined from the astrometric alignment adjustments between Gaia to HST with 1000 stars and HST to JWST with four stars, where we take the error on the mean for each and add them in quadrature. This work marks the first time an extragalactic low-metallicity PDR has ever been resolved.

### 5.1. Comparison to PDR Models

We compared our results to a constant-pressure ($P_{th}/k \sim 7.6 \times 10^6$ K cm$^{-3}$) SMC PDR model, convolving the model line emissivities to match the $H_2$ 2.12 $\mu$m, [C I], and CO resolutions using a Gaussian kernel at the spatial resolution of each individual line. The convolved models were then overlaid on our radial profiles shown in Figure 4. We also show a constant-density ($n = 3.9 \times 10^4$ cm$^{-3}$) PDR model for comparison.

Since the observed position of the DF from the $H_2$ 1–0 S(1) line is well defined and the models have an arbitrary $x$ location, we shift the peak in the models to match the observed peak to compare the spacing of the boundaries. This adds one constant spatial shift to the models and does not change the spacing between the model peaks.

Our results show that the constant-density models overestimate the $H_2$ to C/CO separation by $\sim 1''$ as presented in Table 1. In contrast, the constant-pressure models fit the observed spacings well, reproducing the separations between the H/$H_2$ and the C/CO transition as well as the coincidence of [C I] and CO emission at our resolution. The best-fit pressure is only $\sim 35\%$ higher than (and consistent within the uncertainties of) an estimate of the thermal pressure in the adjacent ionized gas ($P_{th}/k = 5.6 \times 10^6$ K cm$^{-3}$) from electron density measurements using low-angular-resolution Spitzer spectroscopy of [S III] (K. M. Sandstrom et al. 2012) and a temperature of $T_e \sim 12{,}500$ K (e.g., R. J. Dufour & W. V. Harlow 1977). The separation of peaks scales as $1/P_{th}$ for pressures within a factor of 2 of the best fit with a similar dependence for $A_V/N_H$. Changes in

the cosmic-ray ionization rate by a factor of 2 have a negligible effect on the peak separations.

We also note that our fitted $P_{th}$ at $G_0 \sim 10^3$ is somewhat lower than that in C. Joblin et al. (2018) based on high-$J$ CO lines measured in Milky Way PDRs, but is close to the fit in R. Wu et al. (2018) and Y. M. Seo et al. (2019) for an H II region in thermal pressure equilibrium with a surrounding PDR at the Strömgren radius. The pressure is higher than that shown in M. G. Wolfire et al. (2022, their Figure 13) for a compilation of extragalactic observations, possibly due to our much higher spatial resolution, which avoids beam averaging over environments.

### 5.2. Other Resolved PDRs in the Milky Way

Compared to Milky Way PDRs, we observe notable differences in the separation between the H/H$_2$ and C/CO boundaries. In the Orion Bar, J. R. Goicoechea et al. (2016, 2025) find an H/H$_2$ to C/CO boundary separation of $\sim$0.002 pc, which is around 25 times smaller than in N13. Similarly, in the Horsehead Nebula, C. Hernández-Vera et al. (2023) finds a separation of $\lesssim$0.004 pc or 830 au with a $G_0$ of $\sim$100. In both of these PDRs, a constant-pressure model best describes the observed structure. When compared to N13, with a separation of $\sim$0.043 pc, our analysis highlights that PDRs are much more extended and CO-dark H$_2$ gas plays a more prominent role in lower-metallicity environments. We confirm the long-standing theory that the extent of the CO-dark H$_2$ layer increases at low metallicities (A. D. Bolatto et al. 2013; S. C. O. Glover & P. C. Clark 2016; S. C. Madden et al. 2020). In Orion, E. Habart et al. (2024) also find the spatial extent from the IF to DF to be 0.02–0.04 pc. This separation is similar to N13 at $0.025 \pm 0.009$ pc.

Interestingly, the 3.3 $\mu$m feature in N13 shows a fundamental difference to the Orion Bar PDR. In N13, this PAH feature peaks close to the DF at $0\rlap{.}''016 \pm 0\rlap{.}''008$ behind the H$_2$ 2.12 $\mu$m peak. In the Orion Bar, E. Peeters et al. (2024) finds clear bright peaks of the 3.3 $\mu$m feature toward the IF and fainter peaks slightly behind the DF. The differences between Orion and N13 could be caused by a metallicity effect, potentially due to higher penetration of FUV photons from the lack of dust shielding. However, further work is needed to confirm whether metallicity is the primary driver of this difference.

### 5.3. Inclination and Geometry Effects

We examined N13 for inclination effects to see whether the PDR orientation impacts the measured separations between the DF and the C/CO transition. Ideally, the PDR should be at near edge-on inclination (i.e., $\sim$0°), where a well-defined DF and maximally separated boundaries are expected.

We tested the constant-density and constant-pressure models, scaling the separations of different layers by $\sin(i)$ for 0°–90° inclinations $i$ between the line of sight and the PDR surface. The $n = 3.9 \times 10^4$ cm$^{-3}$ constant-density model requires an unrealistic inclination of $\sim$80° to match the observed separations (i.e., a nearly face-on PDR), inconsistent with the visual appearance in HST data showing an approximately edge-on geometry. In contrast, the constant-pressure models match the observations better, with an inclination of $\lesssim$30°.

In addition to the inclination of the individual PDR front, the overall geometry of the region is also of interest in explaining the existence of multiple DFs. In the Orion Bar, E. Habart et al. (2024) similarly finds multiple DFs, which they attribute to terraced structure with three steps to explain the succession of

H$_2$ ridges across the bar, along with an inclination of the bar at 1°–8° (F. Salgado et al. 2016). This could indicate that N13 has a geometry similar to Orion with possibly two terraced surfaces along with a slight tilt. Large-scale geometry effects likely explain the presence of two DFs, as our analysis indicates a small inclination for the constant-pressure model.

### 5.4. Clumpy PDRs

Unresolved clumpy structures have been used to explain the overlap of CO and [C I] emission in some PDRs (M. Cubick et al. 2008). Physical drivers, like turbulence, can create a multiphase clumpy medium with uneven radiation penetration, increasing the temperature deeper in the PDR, and enhancing chemical processes (S. C. O. Glover et al. 2015). If the PDR was clumpy, CO clumps could remain unresolved in our observations (at $\lesssim$0.075 pc). Our results do show nearly cospatial $^{12}$CO $J = 2-1$, $J = 3-2$, and [C I] $1-0$. This implies a potentially clumpy gas distribution, although this type of model may not accurately match the separation of the H$_2$ and C/CO layers. Due to uncertainty in whether a clumpy model would match all the observed spacings, we cannot dismiss the possibility of a clumpy structure based solely on the observed spacing of the [C I] and CO species.

Another way to constrain the presence of subresolution clumps is to use the peak temperature from optically thick CO emission. This peak temperature may not represent the actual gas temperature if the clumps are still unresolved, as the expected peak $T_{pk}$ for optically thick CO is much lower than the actual gas temperature in these cases.[23] If we observe a much lower $T_{pk}$, it may be consistent with clumpiness as an explanation for the almost cospatial overlap of CO/CI.

To test if clumps play a role in the PDR structure of N13, we create a linear radial profile of the CO peak temperature maps produced from the PHANGS-ALMA pipeline (discussed in Section 2.3). We compare the peak temperature radial slice to the emission-weighted gas temperature ($T_{gas}$) from the constant-pressure PDR models for the optically thick $^{12}$CO $J = 2-1$ in Figure 5.

We find that the peak temperature of the $^{12}$CO $J = 2-1$ emission is $\sim$34 K, only $\sim$1 K more than the model predictions for the line. There is strong agreement between the modeled and observed peaks, indicative of a high filling factor and a well-matched model for N13. Additionally, the similar observed peak temperature to the model suggests the absence of subresolution clumps. Alternatively, in regimes with a lower observed peak temperature this may indicate that the CO emission is not filling the entire beam, likely due to a low filling factor caused by unresolved clumps. We note that this offset in the modeled peak temperature could come from PDR model uncertainty, since the temperature structure is most sensitive to potential metallicity-driven variations in the heating and cooling.

The lack of strong evidence for the presence of subresolution clumps from Figure 5, and the sufficient constant-pressure model match to the observed separations of the DF and C/CO transitions, point to the plane-parallel models being adequate to explain the structure of N13. However, models like Kosma-$\tau$ (M. Röllig & V. Ossenkopf-Okada 2022) highlight the need to account for small-scale structures that may be influencing the observed emission patterns. Further exploration of clumpy

---

[23] Additionally, $T_{pk}$ can also be lower than $T_{gas}$ if $n \lesssim n_{critical}$. We found that for the CO $2-1$ transition the densities in the constant-pressure model always exceeded the critical density for collisions with H$_2$.
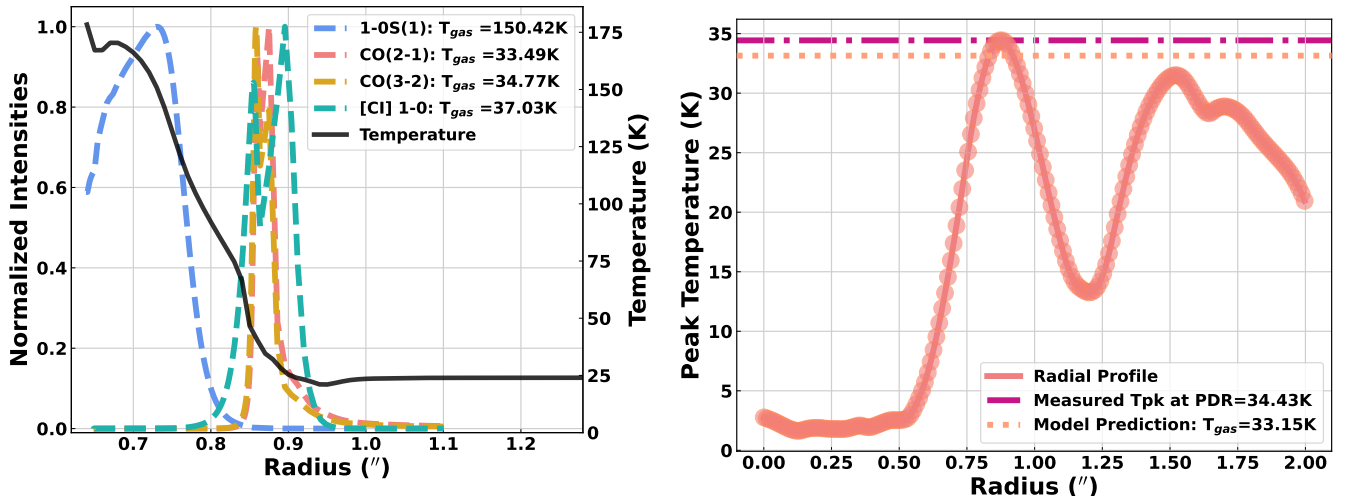
**Figure 5.** In the left panel, we plot the models, the theoretical unconvolved temperature profile across the PDR in a solid black line, and the emissivity of each relevant species in colored dashed lines. The model emission-weighted gas temperature ($T_{gas}$) for each species is listed in the legend. In the right panel, we show the model peak temperature ($T_{gas}$) and the observed optically thick $^{12}$CO $J = 2-1$ peak temperature profile $T_{pk}$.

PDR and constant-pressure models is necessary to disentangle these effects.

### 5.5. CO-dark $H_2$

In low-metallicity environments, where the dust-to-gas ratio is lower (i.e., the $A_V/N_H$ is lower), there is expected to be a higher proportion of CO-dark $H_2$ (S. C. O. Glover & M. M. Mac Low 2011; A. Schruba et al. 2012; A. D. Bolatto et al. 2013; R. Nordon & A. Sternberg 2016; S. C. Madden et al. 2020; T. G. Bisbas et al. 2021; C.-Y. Hu et al. 2021), increasing the uncertainty in calibrating the $X_{CO}$ factor. These lower-metallicity environments in particular lead to deeper UV penetration, typically decreasing the amount of CO that can survive close to the DF. This metallicity effect also leads to a more extended molecular zone (A. D. Bolatto et al. 1999; M. Röllig et al. 2006; N. Schneider et al. 2021), adding further uncertainty on the constraint for the $X_{CO}$ conversion factor. It is important to note that there is also a geometric aspect to the problem where complex filamentary geometry can dramatically increase the expected fraction of CO-dark $H_2$ gas compared to simple plane-parallel or spherical shell models (R. J. Smith et al. 2014).

The separation between the DF and the C/CO transition is observed to be $0.043 \pm 0.013$(stat.) $\pm 0.0036$(syst.) pc, while the predicted separation for the constant-pressure model is 0.045 pc. This corresponds to a modeled CO-dark gas column density of $N_{H_2} \sim 1.1 \times 10^{22}$ cm$^{-2}$. We find that a Galactic PDR with the same incident FUV field and thermal pressure would have a CO-dark gas column density of $N_{H_2} \sim 2.1 \times 10^{21}$ cm$^{-2}$, equivalent to a DF to C/CO separation of $0''04$, or 0.012pc. This difference indicates that the SMC N13 PDR has a CO-dark gas column density 5 times greater than that of a Milky Way PDR. The plane-parallel model depth extends past the observed emission peaks but the total depth is not tied to a specific molecular cloud model, and thus we are unable to obtain a unique $H_2$ column density. Therefore, we cannot calculate a precise value of $X_{CO}$. The typical Galactic $X_{CO}$ factor is $2 \times 10^{20}$ cm$^{-2}$/(K km s$^{-1}$).

It is important to note that, in this case, there are no significant improvements in using [C I] $1-0$ over CO to trace CO-dark $H_2$. In N13, the [C I] $1-0$ emission is not particularly bright in the higher-$A_V$ molecular material traced by CO, as it would be expected if [C I] mostly arises from photodissociation in a thin PDR layer. Therefore, it does not do a good job at capturing the bulk of the CO-emitting molecular gas. Some studies propose [C I] as an alternative to trace molecular gas in regions where CO emission is weak or absent, or even find [C I] a better tracer of $H_2$ than CO in general (M. Gerin & T. G. Phillips 2000; P. P. Papadopoulos et al. 2004; C. Kramer et al. 2008; S. C. O. Glover et al. 2015; T. G. Bisbas et al. 2025). Our results suggest that using [C I] to trace $H_2$, particularly in low-metallicity environments, has limitations. Further exploration of the conditions under which neutral carbon can be a reliable tracer of molecular gas is needed in order to establish its usefulness.

## 6. Conclusions and Implications for Low-metallicity PDRs

For the first time, we have spatially resolved an extragalactic, low-metallicity PDR showcasing the capabilities of the JWST in conjunction with ALMA for studying PDRs in the SMC. We measure our separation for the transition from the DF to the average of the $^{12}$CO $J = 2-1$ and $^{12}$CO $J = 3-2$ peaks to be $0''146 \pm 0''042$(stat.) $\pm 0''012$(syst.) or $0.043 \pm 0.013$ (stat.) $\pm 0.0036$(syst.) pc. Our findings reveal that the N13 PDR has separations between the H/$H_2$ and C/CO transitions consistent with the plane-parallel constant-pressure model at 0.045 pc ($0''150$), while the constant-density model at 0.195 pc ($0''650$), overestimates the separations. A reduced $A_V/N_H$ for SMC conditions is also necessary in the models to match the observed spacings. This reasonable match between the constant-pressure models and our observations suggests that traditional plane-parallel PDR models do a good job describing the spatial extent of the CO-dark $H_2$ in low-metallicity environments. Understanding the spatial extent of CO-dark gas is crucial for refining the $X_{CO}$ conversion factor, highlighting the role CO-dark $H_2$ plays in the ISM of low-metallicity galaxies, which resemble conditions in the early Universe. The PDR model that describes N13 has a CO-dark $H_2$ column density 5 times higher than the comparable Milky Way model.

Understanding the mechanisms driving PDR structure at low metallicity is critical for tracing molecular gas and understanding the evolution of the ISM throughout the early Universe. Future efforts for N13 will explore the impact of the

spectrum of the ionizing OB stars on the PDR, the temperature structure of the neutral gas using the $H_2$ rotational ladder and CO spectral line energy distribution, and the nature of the small dust grain population, in addition to improving models to better describe metallicity-driven changes. We present the first resolved extragalactic and low-metallicity PDR. However, a larger sample of low-metallicity PDRs with submillimeter and infrared data is essential for placing robust constraints on state-of-the-art PDR models and for improving our understanding of low-metallicity astrochemistry.

### Appendix
### PDR Models and Resulting Profiles

In the top panel of Figure 6, we present the abundance profiles for the constant-pressure model that shows the best correspondence with the observations of the N13 PDR. In the figure $x_i = n_i/n$ is the fractional abundance of species $i$ and $A_C = 3.2 \times 10^{-5}$ is the gas-phase abundance of carbon per hydrogen nucleus. The profiles are scaled by constant factors to be shown on the same plot (e.g., $C^+$/C/CO are scaled by $1/A_C$). In the middle panel of this figure, we show the constant-pressure model with unconvolved (solid) and convolved (dashed) emissivity profiles to match our resolution. In this panel, we present the emissivity profiles of the $H_2$ 2.12 $\mu$m, [C I] 1–0, $^{12}$CO $J = 2-1$, and $^{12}$CO $J = 3-2$ lines. In the bottom panel of Figure 6, we present the temperature profile for the constant-pressure model. Vertical dotted–dashed gray lines in both panels show the observed locations of the IF, DF, and C/CO transitions from left to right in both panels. We find the constant-pressure model abundance profiles show a close agreement between the transition locations and the observed emission peaks, which we assign to the DF and C/CO transition. In the convolved constant-pressure model, the separation between the peak of CO $J = 2-1$ and [C I] 1–0 is 0.006 pc, corresponding to 0.4 $A_v$. We note that the abundance profiles are not convolved to match the resolution of the observations. In addition, the constant-pressure model also does a reasonable job of reproducing the IF location (the model curves end at the IF).

The models calculate the $H_2$ excitation and emission using 150 $vj$ levels. The radiative transition coefficients are taken from E. Roueff et al. (2019). Collision coefficients for collisions with atomic H, o–$H_2$, and p–$H_2$ are taken from S. A. Wrathmall et al. (2007), and D. R. Flower & E. Roueff (1998, 1999). For CO, we use a maximum of 40 rotational levels with $A$ values from S. Chandra et al. (1996) and collision rates with o–$H_2$ and p–$H_2$ from B. Yang et al. (2010). The line emissivity is computed following Equations (B1), (B2), and (B3) in A. G. G. M. Tielens & D. Hollenbach (1985), with the line optical depth and escape probability as in (B8) and (B9). The model 1–0 S(1) emissivity peaks at the DF, where the gas mass is half-molecular and is
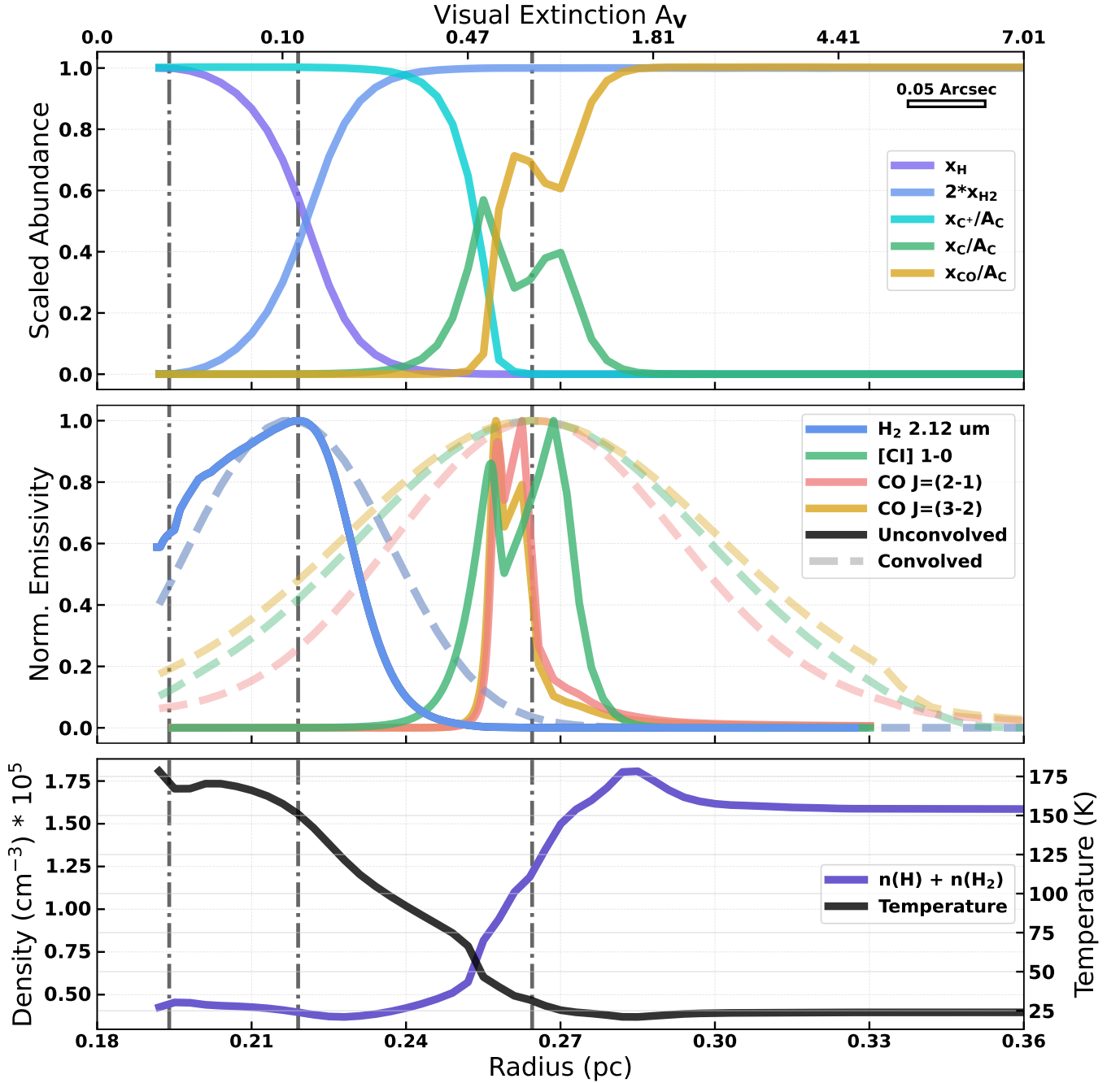
**Figure 6.** Top panel: we present the scaled radial abundance profiles of the $P_{th}/k = 7.6 \times 10^6$ K cm$^{-3}$ constant-pressure model, where $x_i = n_i/n$ is the fractional abundance of species $i$ and $A_C = 3.2 \times 10^{-5}$ is the gas-phase abundance of carbon per hydrogen nucleus. To show all profiles on the same plot while preserving their shapes, we scale the H$_2$ fractional abundance by 2 and the C$^+$/C/CO profiles by $1/A_C$. Half of the gas is molecular H$_2$ at $2x_{H2} = 0.5$. Middle panel: we present the unconvolved (solid) and convolved (dashed) emissivity profiles of the H$_2$ 2.12$\mu$m, [C I] 1–0, $^{12}$CO $J = 2-1$, and $^{12}$CO $J = 3-2$ lines from the constant-pressure model mentioned in the top panel. Bottom panel: we show the modeled temperature profile along with the H+H$_2$ density profile across the PDR for the constant-pressure case as presented in the top panel. We identify the IF, the DF, and the C/CO transition, from left to right, as seen in the vertical dashed–dotted gray lines in each panel.

excited by FUV pumping. There, gas heating is dominated by photoelectric heating with some contribution from H$_2$ formation heating and balanced by mainly [O I] 63 $\mu$m fine-structure line cooling. The CO emission peaks at the edge of the C/CO transition, where the CO abundance starts to rise while the gas temperature is still sufficiently warm to excite the CO transitions. There, heating is dominated by photoelectric heating and balanced by mainly CO rotational line cooling.

We note that the observed 1–0 S(1) line emission exhibits a peak at the model DF. The observed 1–0 S(1)/2−1 S(1) ratio at the peak is ~2.2, confirming that the emission is due to FUV pumping. In steady state, the H$_2$ FUV pumping rate is proportional to the H$_2$ formation rate on grains $Rnn_{H\,I}$, where $R$ is the formation rate coefficient, and $n_{H\,I}$ is the atomic hydrogen density. One would expect, in the limit of constant $R$ and $n$, that the emission would simply follow the atomic hydrogen density and there would

| R.A. (hh:mm:ss) | Decl. (deg:arcmin:arcsec) | Radii (arcsec) | H₂ 2.12 μm (erg s⁻¹ cm⁻² sr⁻¹ × 10⁻⁵) | CO $J = 2–1$ (K km s⁻¹) | CO $J = 3–2$ (K km s⁻¹) | [C I] 1–0 (K km s⁻¹) |
|---|---|---|---|---|---|---|
| 0: 45: 26.913 | −73: 22: 55.129 | 1.57 | 1.40 ± 0.03 | 38.45 ± 0.55 | 42.18 ± 0.36 | 4.85 ± 0.02 |
| 0: 45: 26.915 | −73: 22: 55.122 | 1.58 | 1.36 ± 0.04 | 37.81 ± 0.55 | 41.58 ± 0.43 | 4.93 ± 0.02 |
| 0: 45: 26.917 | −73: 22: 55.116 | 1.59 | 1.32 ± 0.04 | 37.18 ± 0.57 | 40.98 ± 0.49 | 5.00 ± 0.02 |
| 0: 45: 26.918 | −73: 22: 55.110 | 1.60 | 1.30 ± 0.04 | 36.53 ± 0.59 | 40.36 ± 0.55 | 5.05 ± 0.02 |
| 0: 45: 26.920 | −73: 22: 55.103 | 1.61 | 1.30 ± 0.04 | 35.88 ± 0.60 | 39.72 ± 0.60 | 5.08 ± 0.02 |
| 0: 45: 26.922 | −73: 22: 55.097 | 1.62 | 1.31 ± 0.05 | 35.23 ± 0.60 | 39.06 ± 0.64 | 5.09 ± 0.04 |
| 0: 45: 26.924 | −73: 22: 55.091 | 1.63 | 1.34 ± 0.05 | 34.59 ± 0.58 | 38.39 ± 0.68 | 5.07 ± 0.06 |
| 0: 45: 26.926 | −73: 22: 55.084 | 1.64 | 1.38 ± 0.05 | 33.93 ± 0.56 | 37.70 ± 0.71 | 5.02 ± 0.09 |
| 0: 45: 26.927 | −73: 22: 55.078 | 1.65 | 1.43 ± 0.04 | 33.23 ± 0.54 | 37.00 ± 0.75 | 4.93 ± 0.12 |
| 0: 45: 26.929 | −73: 22: 55.072 | 1.66 | 1.48 ± 0.04 | 32.52 ± 0.53 | 36.28 ± 0.78 | 4.82 ± 0.12 |
| 0: 45: 26.931 | −73: 22: 55.065 | 1.67 | 1.52 ± 0.04 | 31.80 ± 0.52 | 35.55 ± 0.81 | 4.70 ± 0.11 |
| 0: 45: 26.933 | −73: 22: 55.059 | 1.68 | 1.56 ± 0.04 | 31.03 ± 0.54 | 34.82 ± 0.84 | 4.58 ± 0.10 |
| 0: 45: 26.935 | −73: 22: 55.053 | 1.69 | 1.57 ± 0.03 | 30.28 ± 0.57 | 34.10 ± 0.86 | 4.45 ± 0.10 |
| 0: 45: 26.937 | −73: 22: 55.046 | 1.70 | 1.57 ± 0.02 | 29.76 ± 0.53 | 33.37 ± 0.86 | 4.31 ± 0.10 |
| 0: 45: 26.938 | −73: 22: 55.040 | 1.71 | 1.52 ± 0.01 | 29.37 ± 0.48 | 32.65 ± 0.86 | 4.18 ± 0.11 |
| 0: 45: 26.940 | −73: 22: 55.034 | 1.72 | 1.45 ± 0.00 | 29.01 ± 0.44 | 31.93 ± 0.86 | 4.06 ± 0.12 |
| 0: 45: 26.942 | −73: 22: 55.027 | 1.73 | 1.39 ± 0.00 | 28.66 ± 0.42 | 31.21 ± 0.84 | 3.93 ± 0.13 |
| 0: 45: 26.944 | −73: 22: 55.021 | 1.74 | 1.35 ± 0.01 | 28.30 ± 0.41 | 30.50 ± 0.83 | 3.82 ± 0.15 |
| 0: 45: 26.946 | −73: 22: 55.015 | 1.75 | 1.32 ± 0.01 | 27.89 ± 0.42 | 29.79 ± 0.81 | 3.72 ± 0.17 |
| 0: 45: 26.947 | −73: 22: 55.008 | 1.76 | 1.30 ± 0.01 | 27.43 ± 0.43 | 29.09 ± 0.80 | 3.64 ± 0.18 |
| 0: 45: 26.949 | −73: 22: 55.002 | 1.77 | 1.31 ± 0.01 | 26.93 ± 0.43 | 28.40 ± 0.78 | 3.57 ± 0.17 |
| 0: 45: 26.951 | −73: 22: 54.996 | 1.78 | 1.35 ± 0.01 | 26.39 ± 0.42 | 27.73 ± 0.77 | 3.49 ± 0.16 |
| 0: 45: 26.953 | −73: 22: 54.990 | 1.79 | 1.38 ± 0.00 | 25.81 ± 0.40 | 27.07 ± 0.76 | 3.39 ± 0.16 |
| 0: 45: 26.955 | −73: 22: 54.983 | 1.80 | 1.40 ± 0.00 | 25.19 ± 0.39 | 26.42 ± 0.76 | 3.30 ± 0.15 |
| 0: 45: 26.957 | −73: 22: 54.977 | 1.81 | 1.43 ± 0.00 | 24.51 ± 0.36 | 25.77 ± 0.75 | 3.19 ± 0.15 |
| 0: 45: 26.958 | −73: 22: 54.971 | 1.82 | 1.44 ± 0.01 | 23.80 ± 0.33 | 25.14 ± 0.74 | 3.07 ± 0.14 |
| 0: 45: 26.960 | −73: 22: 54.964 | 1.83 | 1.45 ± 0.02 | 23.04 ± 0.32 | 24.52 ± 0.74 | 2.95 ± 0.14 |
| 0: 45: 26.962 | −73: 22: 54.958 | 1.84 | 1.45 ± 0.02 | 22.24 ± 0.32 | 23.91 ± 0.72 | 2.81 ± 0.13 |
| 0: 45: 26.964 | −73: 22: 54.952 | 1.85 | 1.44 ± 0.03 | 21.43 ± 0.30 | 23.35 ± 0.70 | 2.67 ± 0.13 |
| 0: 45: 26.966 | −73: 22: 54.945 | 1.86 | 1.43 ± 0.03 | 20.72 ± 0.26 | 22.78 ± 0.67 | 2.51 ± 0.13 |
| 0: 45: 26.967 | −73: 22: 54.939 | 1.87 | 1.42 ± 0.04 | 20.07 ± 0.24 | 22.22 ± 0.65 | 2.35 ± 0.12 |
| 0: 45: 26.969 | −73: 22: 54.933 | 1.88 | 1.43 ± 0.05 | 19.40 ± 0.23 | 21.65 ± 0.62 | 2.18 ± 0.11 |

**Note.** We present the last 30 rows of our measured radial profiles along Slice 1 for H₂ 2.12 μm, CO $J = 2–1$, CO $J = 3–2$, and [C I] 1–0. The second row of the table header indicates the units and the third column indicates the scaling factor for the number in that column. The H₂ 2.12 μm is scaled as $10^{-5}$ for readability, and is in units of erg s⁻¹ cm⁻² sr⁻¹, while the [C I] 1–0 and CO lines are not scaled and in units of K Km s⁻¹.

(This table is available in its entirety in machine-readable form in the online article.)

not be a peak in emission. However, there are several additional processes that affect the line profile.

At depths into the cloud before the peak, photo-processes can suppress the abundance of vibrationally excited H₂ in $v = 1$, $j = 3$ whenever the photo rates are comparable to radiative deexcitation to ground (e.g., M. G. Burton et al. 1990). With increasing column density, H₂ self-shielding reduces the photo depopulation of excited H₂ in $v = 1$, $j = 3$, causing a rise in H₂ 1–0 S(1) line emission. Increasing self-shielding in the lower H₂ rotational levels reduces the FUV pumping and causes a drop on the far side of the peak. The rise in H₂ abundance is a result of the same H₂ self-shielding. As a result, the 1–0 S(1) line appears as a peak in emission closely associated with the H₂ DF. In addition, in constant-pressure models, a rapidly rising gas temperature toward the cloud surface reduces both $n$ and $n_H$, causing a rapid drop in the H₂ formation rate and, in steady state, a drop in the FUV pumping rate.

Models also predict a peak in the 1–0 S(1) line at the DF when collisional excitation dominates the 1–0 S(1) line emission (see, e.g., M. G. Burton et al. 1990, Figure 1; K. N. Allers et al. 2005, Figure 6; J. R. Goicoechea et al. 2019, Figure 10). The high gas temperature, combined with the increasing H₂ fraction, produces a peak that falls off when the gas temperature drops. We suggest the 1–0 S(1) emission peak at the DF occurs for a wide range of conditions for both collisionally excited and FUV-pumped excitation, however for $G_0$ much less than ∼1000, and for FUV pumping, the peak will likely to be minor since photo depopulation will no longer compete with downward radiative deexcitation.
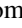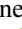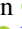
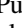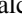More recent updates to PDR models include the photo-dissociation and photoionization rates from A. N. Heays et al. (2017), ¹³C chemistry, measured dissociative recombination rates of OH⁺ (Á. Kálosi et al. 2023) and CH⁺ (D. Paul et al. 2022), and collisional excitation of C by H₂ (J. Kłos et al. 2021; J. R. Goicoechea et al. 2025).

**Table 3**
Radial Profile Data: PAH 3.3 $\mu$m, H I Paschen 4–3, and H I Brackett 5–4

| R.A. (hh:mm:ss) | Decl. (deg:arcmin:arcsec) | Radii (arcsec) | PAH 3.3$\mu$m (erg s$^{-1}$ cm$^{-2}$ sr$^{-1}$ $\times$ 10$^{-5}$) | Paschen 4–3 (erg s$^{-1}$ cm$^{-2}$ sr$^{-1}$ $\times$ 10$^{-5}$) | Brackett 5–4 (erg s$^{-1}$ cm$^{-2}$ sr$^{-1}$) |
|---|---|---|---|---|---|
| 0: 45: 26.915 | −73: 22: 55.122 | 1.57 | 11.70 $\pm$ 0.05 | 30.33 $\pm$ 0.20 | 8.27 $\pm$ 0.03 |
| 0: 45: 26.917 | −73: 22: 55.116 | 1.58 | 11.64 $\pm$ 0.07 | 30.17 $\pm$ 0.19 | 8.24 $\pm$ 0.03 |
| 0: 45: 26.918 | −73: 22: 55.110 | 1.59 | 11.57 $\pm$ 0.05 | 29.94 $\pm$ 0.14 | 8.18 $\pm$ 0.03 |
| 0: 45: 26.920 | −73: 22: 55.103 | 1.60 | 11.44 $\pm$ 0.03 | 29.55 $\pm$ 0.09 | 8.12 $\pm$ 0.03 |
| 0: 45: 26.922 | −73: 22: 55.097 | 1.61 | 11.39 $\pm$ 0.03 | 29.20 $\pm$ 0.07 | 8.04 $\pm$ 0.03 |
| 0: 45: 26.924 | −73: 22: 55.091 | 1.62 | 11.35 $\pm$ 0.04 | 28.71 $\pm$ 0.02 | 7.95 $\pm$ 0.02 |
| 0: 45: 26.926 | −73: 22: 55.084 | 1.63 | 11.28 $\pm$ 0.06 | 28.18 $\pm$ 0.02 | 7.87 $\pm$ 0.03 |
| 0: 45: 26.927 | −73: 22: 55.078 | 1.64 | 11.22 $\pm$ 0.10 | 27.72 $\pm$ 0.05 | 7.81 $\pm$ 0.03 |
| 0: 45: 26.929 | −73: 22: 55.072 | 1.65 | 11.20 $\pm$ 0.15 | 27.31 $\pm$ 0.08 | 7.77 $\pm$ 0.03 |
| 0: 45: 26.931 | −73: 22: 55.065 | 1.66 | 11.23 $\pm$ 0.21 | 26.94 $\pm$ 0.10 | 7.73 $\pm$ 0.02 |
| 0: 45: 26.933 | −73: 22: 55.059 | 1.67 | 11.34 $\pm$ 0.27 | 26.63 $\pm$ 0.11 | 7.70 $\pm$ 0.02 |
| 0: 45: 26.935 | −73: 22: 55.053 | 1.68 | 11.58 $\pm$ 0.34 | 26.40 $\pm$ 0.10 | 7.66 $\pm$ 0.01 |
| 0: 45: 26.937 | −73: 22: 55.046 | 1.69 | 12.06 $\pm$ 0.41 | 26.31 $\pm$ 0.06 | 7.62 $\pm$ 0.00 |
| 0: 45: 26.938 | −73: 22: 55.040 | 1.70 | 12.71 $\pm$ 0.41 | 26.52 $\pm$ 0.02 | 7.59 $\pm$ 0.01 |
| 0: 45: 26.940 | −73: 22: 55.034 | 1.71 | 13.39 $\pm$ 0.40 | 26.96 $\pm$ 0.01 | 7.54 $\pm$ 0.02 |
| 0: 45: 26.942 | −73: 22: 55.027 | 1.72 | 13.71 $\pm$ 0.39 | 27.31 $\pm$ 0.01 | 7.50 $\pm$ 0.02 |
| 0: 45: 26.944 | −73: 22: 55.021 | 1.73 | 13.75 $\pm$ 0.36 | 27.58 $\pm$ 0.01 | 7.48 $\pm$ 0.03 |
| 0: 45: 26.946 | −73: 22: 55.015 | 1.74 | 13.77 $\pm$ 0.34 | 27.86 $\pm$ 0.01 | 7.47 $\pm$ 0.03 |
| 0: 45: 26.947 | −73: 22: 55.008 | 1.75 | 14.17 $\pm$ 0.34 | 28.05 $\pm$ 0.03 | 7.45 $\pm$ 0.04 |
| 0: 45: 26.949 | −73: 22: 55.002 | 1.76 | 14.87 $\pm$ 0.35 | 28.20 $\pm$ 0.04 | 7.42 $\pm$ 0.04 |
| 0: 45: 26.951 | −73: 22: 54.996 | 1.77 | 15.48 $\pm$ 0.33 | 28.36 $\pm$ 0.04 | 7.41 $\pm$ 0.04 |
| 0: 45: 26.953 | −73: 22: 54.990 | 1.78 | 15.86 $\pm$ 0.27 | 28.46 $\pm$ 0.05 | 7.39 $\pm$ 0.04 |
| 0: 45: 26.955 | −73: 22: 54.983 | 1.79 | 16.01 $\pm$ 0.24 | 28.47 $\pm$ 0.07 | 7.39 $\pm$ 0.04 |
| 0: 45: 26.957 | −73: 22: 54.977 | 1.80 | 16.07 $\pm$ 0.24 | 28.40 $\pm$ 0.07 | 7.38 $\pm$ 0.04 |
| 0: 45: 26.958 | −73: 22: 54.971 | 1.81 | 16.07 $\pm$ 0.26 | 28.27 $\pm$ 0.07 | 7.38 $\pm$ 0.04 |
| 0: 45: 26.960 | −73: 22: 54.964 | 1.82 | 16.04 $\pm$ 0.29 | 28.10 $\pm$ 0.06 | 7.38 $\pm$ 0.04 |
| 0: 45: 26.962 | −73: 22: 54.958 | 1.83 | 16.25 $\pm$ 0.20 | 27.91 $\pm$ 0.04 | 7.37 $\pm$ 0.04 |
| 0: 45: 26.964 | −73: 22: 54.952 | 1.84 | 16.38 $\pm$ 0.16 | 27.73 $\pm$ 0.02 | 7.36 $\pm$ 0.04 |
| 0: 45: 26.966 | −73: 22: 54.945 | 1.85 | 16.50 $\pm$ 0.14 | 27.59 $\pm$ 0.01 | 7.35 $\pm$ 0.04 |
| 0: 45: 26.967 | −73: 22: 54.939 | 1.86 | 16.55 $\pm$ 0.12 | 27.48 $\pm$ 0.01 | 7.33 $\pm$ 0.03 |
| 0: 45: 26.969 | −73: 22: 54.933 | 1.87 | 16.46 $\pm$ 0.12 | 27.45 $\pm$ 0.01 | 7.34 $\pm$ 0.03 |

**Note.** Continuation of Table 2. We present the last 30 rows of the measured radial profiles along Slice 1 for PAH 3.3 $\mu$m, H I Paschen 4–3, and H I Brackett 5–4. The second row of the table header indicates the units and the third column indicates the scaling factor for the data in that column. The full version is available for download (see Table 2).

## ORCID iDs

Ilyse Y. Clark ⓘ https://orcid.org/0000-0003-3334-4267
Karin Sandstrom ⓘ https://orcid.org/0000-0002-4378-8534
Mark Wolfire ⓘ https://orcid.org/0000-0003-0030-9510
Alberto D. Bolatto ⓘ https://orcid.org/0000-0002-5480-5686
Jérémy Chastenet ⓘ https://orcid.org/0000-0002-5235-5589
Daniel A. Dale ⓘ https://orcid.org/0000-0002-5782-9093
Brandt A. L. Gaches ⓘ https://orcid.org/0000-0003-4224-6829
Simon C. O. Glover ⓘ https://orcid.org/0000-0001-6708-1317
Javier R. Goicoechea ⓘ https://orcid.org/0000-0001-7046-4319
Karl D. Gordon ⓘ https://orcid.org/0000-0001-5340-6774
Brent Groves ⓘ https://orcid.org/0000-0002-9768-0246
Lindsey Hands ⓘ https://orcid.org/0009-0005-0750-2956
Ralf Klessen ⓘ https://orcid.org/0000-0002-0560-3172
Ilse De Looze ⓘ https://orcid.org/0000-0001-9419-6355
J. D. T. Smith ⓘ https://orcid.org/0000-0003-1545-5078
Dries Van De Putte ⓘ https://orcid.org/0000-0002-5895-8268
Stefanie K. Walch ⓘ https://orcid.org/0000-0001-6941-7638

## References

Abdo, A. A., Ackermann, M., Ajello, M., et al. 2010, A&A, 523, A46
Allers, K. N., Jaffe, D. T., Lacy, J. H., Draine, B. T., & Richter, M. J. 2005, ApJ, 630, 368
Argyriou, I., Glasse, A., Law, D. R., et al. 2023, A&A, 675, A111
Astropy Collaboration, Price-Whelan, A. M., Lim, P. L., et al. 2022, ApJ, 935, 167
Astropy Collaboration, Price-Whelan, A. M., Sipőcz, B. M., et al. 2018, AJ, 156, 123
Astropy Collaboration, Robitaille, T. P., Tollerud, E. J., et al. 2013, A&A, 558, A33
Bakes, E. L. O., & Tielens, A. G. G. M. 1994, ApJ, 427, 822
Bell, T. A., Viti, S., & Williams, D. A. 2007, MNRAS, 378, 983
Bellomi, E., Godard, B., Hennebelle, P., et al. 2020, A&A, 643, A36
Bialy, S., & Sternberg, A. 2019, ApJ, 881, 160
Bisbas, T. G., Bell, T. A., Viti, S., Yates, J., & Barlow, M. J. 2012, MNRAS, 427, 2100
Bisbas, T. G., Haworth, T. J., Barlow, M. J., et al. 2015, MNRAS, 454, 2828
Bisbas, T. G., Tan, J. C., & Tanaka, K. E. I. 2021, MNRAS, 502, 2701
Bisbas, T. G., Zhang, Z.-Y., Gjergo, E., et al. 2024, MNRAS, 527, 8886
Bisbas, T. G., Zhang, Z.-Y., Kyrmanidou, M.-C., et al. 2025, A&A, 697, A115
Böker, T., Arribas, S., Lützgendorf, N., et al. 2022, A&A, 661, A82
Bolatto, A. D., Jackson, J. M., & Ingalls, J. G. 1999, ApJ, 513, 275
Bolatto, A. D., Leroy, A. K., Jameson, K., et al. 2011, ApJ, 741, 12
Bolatto, A. D., Wolfire, M., & Leroy, A. K. 2013, ARA&A, 51, 207
Bradley, L., Sipőcz, B., Robitaille, T., et al. 2023, astropy/photutils: v1.8.0, Zenodo, doi:10.5281/zenodo.7946442
Bron, E., Daudon, C., Pety, J., et al. 2018, A&A, 610, A12
Burton, M. G., Hollenbach, D. J., & Tielens, A. G. G. M. 1990, ApJ, 365, 620
Bushouse, H., Eisenhamer, J., Dencheva, N., et al. 2024, JWST Calibration Pipeline, v1.16.1, Zenodo, doi:10.5281/zenodo.14153298
Chandra, S., Maheshwari, V. U., & Sharma, A. K. 1996, A&AS, 117, 557
Chastenet, J., Sandstrom, K., Chiang, I.-D., et al. 2019, ApJ, 876, 62
Chown, R., Sidhu, A., Peeters, E., et al. 2024, A&A, 685, A75

Comrie, A., Wang, K.-S., Hsu, S.-C., et al. 2021, CARTA: The Cube Analysis and Rendering Tool for Astronomy, v2.0.0, Zenodo, doi:10.5281/zenodo.4905459

Conti, P. S., Crowther, P. A., & Leitherer, C. 2008, From Luminous Hot Stars to Starburst Galaxies (Cambridge: Cambridge Univ. Press)

Cubick, M., Stutzki, J., Ossenkopf, V., Kramer, C., & Röllig, M. 2008, A&A, 488, 623

Draine, B. T. 2011, Physics of the Interstellar and Intergalactic Medium (Princeton, NJ: Princeton Univ. Press)

Dufour, R. J., & Harlow, W. V. 1977, ApJ, 216, 706

Flower, D. R., & Roueff, E. 1998, JPhB, 31, 2935

Flower, D. R., & Roueff, E. 1999, JPhB, 32, 3399

Fuente, A., Roueff, E., Le Petit, F., et al. 2024, A&A, 687, A87

Gaches, B. A. L., Walch, S., Wünsch, R., & Mackey, J. 2023, MNRAS, 522, 4674

Gerin, M., & Phillips, T. G. 2000, ApJ, 537, 644

Glover, S. C. O., & Clark, P. C. 2012, MNRAS, 426, 377

Glover, S. C. O., & Clark, P. C. 2016, MNRAS, 456, 3596

Glover, S. C. O., Clark, P. C., Micic, M., & Molina, F. 2015, MNRAS, 448, 1607

Glover, S. C. O., & Mac Low, M. M. 2011, MNRAS, 412, 337

Gnedin, N. Y., & Draine, B. T. 2014, ApJ, 795, 37

Goicoechea, J. R., Cuadrado, S., Pety, J., et al. 2017, A&A, 601, L9

Goicoechea, J. R., Pety, J., Cuadrado, S., et al. 2016, Natur, 537, 207

Goicoechea, J. R., Pety, J., Cuadrado, S., et al. 2025, A&A, 696, A100

Goicoechea, J. R., Santa-Maria, M. G., Bron, E., et al. 2019, A&A, 622, A91

Goldsmith, P. F., Heyer, M., Narayanan, G., et al. 2008, ApJ, 680, 428

Gong, M., Ostriker, E. C., Kim, C.-G., & Kim, J.-G. 2020, ApJ, 903, 142

Gordon, K. D., Clayton, G. C., Misselt, K. A., Landolt, A. U., & Wolff, M. J. 2003, ApJ, 594, 279

Gordon, K. D., Fitzpatrick, E. L., Massa, D., et al. 2024, ApJ, 970, 51

Gorti, U., & Hollenbach, D. 2002, ApJ, 573, 215

Grassi, T., Bovino, S., Schleicher, D. R. G., et al. 2014, MNRAS, 439, 2386

Grenier, I. A., Casandjian, J.-M., & Terrier, R. 2005, Sci, 307, 1292

Gurman, A., Hu, C.-Y., Sternberg, A., & van Dishoeck, E. F. 2024, ApJ, 965, 179

Habart, E., Peeters, E., Berné, O., et al. 2024, A&A, 685, A73

Habing, H. J. 1968, BAN, 19, 421

Haid, S., Walch, S., Seifried, D., et al. 2019, MNRAS, 482, 4062

Harris, C. R., Millman, K. J., van der Walt, S. J., et al. 2020, Natur, 585, 357

Heays, A. N., Bosman, A. D., & van Dishoeck, E. F. 2017, A&A, 602, A105

Hernández-Vera, C., Guzmán, V. V., Goicoechea, J. R., et al. 2023, A&A, 677, A152

Hollenbach, D., Kaufman, M. J., Neufeld, D., Wolfire, M., & Goicoechea, J. R. 2012, ApJ, 754, 105

Hollenbach, D. J., & Tielens, A. G. G. M. 1997, ARA&A, 35, 179

Hollenbach, D. J., & Tielens, A. G. G. M. 1999, RvMP, 71, 173

Hu, C.-Y., Sternberg, A., & van Dishoeck, E. F. 2021, ApJ, 920, 44

Hunter, J. D. 2007, CSE, 9, 90

Israel, F. P. 1997, A&A, 328, 471

Izumi, N., Fukui, Y., Tachihara, K., et al. 2021, PASJ, 73, 174

Jakobsen, P., Ferruit, P., Alves de Oliveira, C., et al. 2022, A&A, 661, A80

Jameson, K. E., Bolatto, A. D., Wolfire, M., et al. 2018, ApJ, 853, 111

Joblin, C., Bron, E., Pinto, C., et al. 2018, A&A, 615, A129

Kálosi, Á., Gamer, L., Grieser, M., et al. 2023, ApJL, 955, L26

Kaufman, M. J., Wolfire, M. G., & Hollenbach, D. J. 2006, ApJ, 644, 283

Kłos, J., Dagdigian, P. J., & Lique, F. 2021, MNRAS, 501, L38

Kramer, C., Cubick, M., Röllig, M., et al. 2008, A&A, 477, 547

Leroy, A. K., Bolatto, A., Gordon, K., et al. 2011, ApJ, 737, 12

Leroy, A. K., Hughes, A., Liu, D., et al. 2021, ApJS, 255, 19

Lupi, A., Bovino, S., Capelo, P. R., Volonteri, M., & Silk, J. 2018, MNRAS, 474, 2884

Madden, S. C., Cormier, D., Hony, S., et al. 2020, A&A, 643, A141

Maillard, V., Bron, E., & Le Petit, F. 2021, A&A, 656, A65

Neufeld, D. A., & Wolfire, M. G. 2016, ApJ, 826, 183

Neufeld, D. A., & Wolfire, M. G. 2017, ApJ, 845, 163

Nordon, R., & Sternberg, A. 2016, MNRAS, 462, 2804

Papadopoulos, P. P., Thi, W. F., & Viti, S. 2004, MNRAS, 351, 147

Parravano, A., Hollenbach, D. J., & McKee, C. F. 2003, ApJ, 584, 797

Paul, D., Grieser, M., Grussie, F., et al. 2022, ApJ, 939, 122

PDRs4AllTeam, Berné, O., Habart, Émilie, et al. 2022, PASP, 134, 054301

Peeters, E., Habart, E., Berné, O., et al. 2024, A&A, 685, A74

Pineda, J. L., Langer, W. D., Velusamy, T., & Goldsmith, P. F. 2013, A&A, 554, A103

Pineda, J. L., Langer, W. D., Goldsmith, P. F., et al. 2017, ApJ, 839, 107

Ramachandran, V., Hamann, W. R., Oskinova, L. M., et al. 2019, A&A, 625, A104

Rémy-Ruyer, A., Madden, S. C., Galliano, F., et al. 2014, A&A, 563, A31

Röllig, M., Ossenkopf, V., Jeyakumar, S., Stutzki, J., & Sternberg, A. 2006, A&A, 451, 917

Röllig, M., & Ossenkopf-Okada, V. 2022, A&A, 664, A67

Roman-Duval, J., Jenkins, E. B., Tchernyshyov, K., et al. 2022, ApJ, 928, 90

Roueff, E., Abgrall, H., Czachorowski, P., et al. 2019, A&A, 630, A58

Saldaño, H. P., Rubio, M., Bolatto, A. D., et al. 2024, A&A, 687, A26

Salgado, F., Berné, O., Adams, J. D., et al. 2016, ApJ, 830, 118

Sandstrom, K. M., Bolatto, A. D., Bot, C., et al. 2012, ApJ, 744, 20

Sandstrom, K. M., Bolatto, A. D., Draine, B. T., Bot, C., & Stanimirović, S. 2010, ApJ, 715, 701

Schneider, N., Röllig, M., Polehampton, E. T., et al. 2021, A&A, 653, A108

Schruba, A., Leroy, A. K., Walter, F., et al. 2012, AJ, 143, 138

Scowcroft, V., Freedman, W. L., Madore, B. F., et al. 2016, ApJ, 816, 49

Seifried, D., Haid, S., Walch, S., Borchert, E. M. A., & Bisbas, T. G. 2020, MNRAS, 492, 1465

Seifried, D., Walch, S., Girichidis, P., et al. 2017, MNRAS, 472, 4797

Seo, Y. M., Goldsmith, P. F., Walker, C. K., et al. 2019, ApJ, 878, 120

Smith, J. D. T., Draine, B. T., Dale, D. A., et al. 2007, ApJ, 656, 770

Smith, R. J., Glover, S. C. O., Clark, P. C., Klessen, R. S., & Springel, V. 2014, MNRAS, 441, 1628

Sternberg, A., & Dalgarno, A. 1995, ApJS, 99, 565

Störzer, H., & Hollenbach, D. 1998, ApJ, 495, 853

Tielens, A. G. G. M. 2010, The Physics and Chemistry of the Interstellar Medium (Cambridge: Cambridge Univ. Press)

Tielens, A. G. G. M., & Hollenbach, D. 1985, ApJ, 291, 722

Toribio San Cipriano, L., Domínguez-Guzmán, G., Esteban, C., et al. 2017, MNRAS, 467, 3759

Van De Putte, D., Meshaka, R., Trahin, B., et al. 2024, A&A, 687, A86

van Dishoeck, E. F., & Black, J. H. 1988, ApJ, 334, 771

Virtanen, P., Gommers, R., Oliphant, T. E., et al. 2020, NatMe, 17, 261

Wolfire, M. G., Hollenbach, D., & McKee, C. F. 2010, ApJ, 716, 1191

Wolfire, M. G., Hollenbach, D., McKee, C. F., Tielens, A. G. G. M., & Bakes, E. L. O. 1995, ApJ, 443, 152

Wolfire, M. G., Vallini, L., & Chevance, M. 2022, ARA&A, 60, 247

Wrathmall, S. A., Gusdorf, A., & Flower, D. R. 2007, MNRAS, 382, 133

Wu, R., Bron, E., Onaka, T., et al. 2018, A&A, 618, A53

Yanchulova Merica-Jones, P., Sandstrom, K. M., Johnson, L. C., et al. 2017, ApJ, 847, 102

Yang, B., Stancil, P. C., Balakrishnan, N., & Forrey, R. C. 2010, ApJ, 718, 1062